Title

Dynamic encounters with red blood cells trigger splenic marginal zone B cell retention and function.

Journal

Nature Immunology, 25(1)

Authors

Winer, Benjamin

Chou, Marissa

Tam, Hanson

et al.

Publication Date

2024

DOI

10.1038/s41590-023-01690-z

Peer reviewed

nature immunology

Article

https://doi.org/10.1038/s41590-023-01690-z

Dynamic encounters with red blood cells trigger splenic marginal zone B cell retention and function

Received: 30 April 2023

Accepted: 24 October 2023

Published online: 4 December 2023

Check for updates

Dan Liu[1,2] ✉, Benjamin Y. Winer[1,3], Marissa Y. Chou[1], Hanson Tam[1], Ying Xu[1], Jinping An[1], James M. Gardner[4] & Jason G. Cyster[1] ✉

Spleen marginal zone (MZ) B cells are important for antibody responses against blood-borne antigens. The signals they use to detect exposure to blood are not well defined. Here, using intravital two-photon microscopy in mice, we observe transient contacts between MZ B cells and red blood cells that are in flow. We show that MZ B cells use adhesion G-protein-coupled receptor ADGRE5 (CD97) for retention in the spleen. CD97 function in MZ B cells depends on its ability to undergo autoproteolytic cleavage and signaling via $G\alpha_{13}$ and ARHGEF1. Red blood cell expression of the CD97 ligand CD55 is required for MZ B cell homeostasis. Applying a pulling force on CD97-transfected cells using an optical C-trap and $CD55^{+}$ beads leads to accumulation of active RhoA and membrane retraction. Finally, we show that CD97 deficiency leads to a reduced T cell-independent IgM response. Thus, our studies provide evidence that MZ B cells use mechanosensing to position in a manner that enhances antibody responses against blood-borne antigens.

The spleen, the largest secondary lymphoid organ, is unique in having an open blood circulation. Central arterioles branch into open-ended terminal arterioles that release blood into the marginal sinus and red pulp[1–3]. Lymphoid regions sheathe the central arterioles and are termed white pulp cords. The interface between the white pulp and the red pulp, known as the marginal zone (MZ), contains a specialized population of MZ B cells as well as macrophages, dendritic cells and stromal cells[1–3]. Blood percolates from the marginal sinus through the MZ before reaching the red pulp and returning to circulation via the venous sinuses. As a result, MZ cells are rapidly exposed to blood-borne antigens. MZ cells are also thought to be extensively exposed to blood-borne cells, but the dynamics of these interactions have not been determined. MZ B cells have a poised, semiactivated state compared to follicular B cells, and they differentiate rapidly into plasma cells following antigen encounter. This property helps provide an early wave of antibodies targeted to blood-borne pathogens[4,5].

Multiple cues act to position MZ B cells. The cells are attracted to the MZ by sphingosine-1-phosphate receptor-1, which responds to S1P that is abundant in blood[6]. Although known for their occupancy of the MZ, MZ B cells are motile and continually shuttle between the MZ and follicle[7,8]. This shuttling contributes to the delivery of blood-borne antigens to follicular dendritic cells for display to follicular B cells. Retention of MZ B cells within the MZ depends on integrin-mediated adhesion, and blockade of integrin function leads to their loss into blood circulation[8,9]. MZ B cell homeostasis also depends on the signaling molecules CNR2, PYK2, BTK, TAOK3 and NOTCH[2,10,11]. Despite this advanced understanding of MZ B cell positioning and homeostasis requirements, the mechanisms that MZ B cells use to sense their location with respect to blood flow are incompletely understood.

Adhesion G-protein-coupled receptors (GPCRs) are a subfamily of GPCRs typified by a long extracellular N-terminal fragment (NTF) and a C-terminal fragment (CTF) that corresponds to the GPCR

[1]Howard Hughes Medical Institute and Department of Microbiology and Immunology, University of California, San Francisco, San Francisco, CA, USA. [2]Westlake Laboratory of Life Sciences and Biomedicine, Westlake University School of Life Sciences, Institute of Basic Medical Sciences and Westlake Institute for Advanced Study, Hangzhou, China. [3]Immunology Program, Memorial Sloan Kettering Cancer Center, New York, NY, USA. [4]Diabetes Center and Department of Surgery, University of California, San Francisco, San Francisco, CA, USA. ✉e-mail: liudan@westlake.edu.cn; jason.cyster@ucsf.edu

domain[12,13]. CD97, or adhesion GPCR E5 (ADGRE5), is a member of the epidermal growth factor (EGF) repeat-containing subgroup of adhesion GPCRs that is widely expressed on hematopoietic cells[12]. Like most adhesion GPCRs, CD97 undergoes autoproteolytic cleavage at the GPCR proteolysis site (GPS) within the GPCR-activation-inducing domain. The NTF and CTF remain noncovalently bound via the GPCR-activation-inducing domain. A theme that has emerged from in vitro studies of several adhesion GPCRs is that their activation can be promoted by force being exerted on the NTF to expose a tethered ligand that is present at the N terminus of the CTF, enabling activation of the receptor[13,14]. The best-defined ligand for the CD97 NTF is the glycosylphosphatidylinositol-anchored membrane protein CD55 (refs. 12,15). Encounters between CD55$^+$ cells and CD97$^+$ cells under shear stress conditions can lead to extraction of the CD97 NTF[16,17]. CD97 and CD55 deficiency are associated with mild granulocytosis and reductions in spleen type 2 conventional dendritic cells[17–20]. However, the cellular changes caused by CD55 engagement of CD97 are not well defined. Moreover, the function of CD97 in other immune cell types is not understood.

Here, using intravital two-photon microscopy of the spleen, we observed interactions between MZ B cells and red blood cells (RBCs) in flow. We found that MZ B cells express high levels of CD97 and depend on this receptor and downstream signaling proteins $G\alpha_{13}$ and ARHGEF1 for their retention and homeostasis. CD97 function was dependent on the expression of CD55 on RBCs, and the NTF of CD97 on both mouse and human MZ B cells was extracted by engagement with CD55$^+$ RBCs under shear stress conditions. Using CD97-transfected HEK293T cells, optical trap measurements showed that pulling forces exerted on CD97 via CD55$^+$ particles caused RhoA activation and cell membrane retraction. CD97 pathway-deficient mice mounted reduced T cell-independent IgM responses against a polysaccharide antigen. These findings support a model where MZ B cell mechanosensation of passing RBCs via CD97–CD55 interaction causes membrane retraction and thus cell retention and function within the spleen.

Results

Intravital imaging reveals MZ B cell–RBC contacts

MZ B cells are distinguished from follicular B cells by high expression of CD21 and IgM and low expression of CD23 and IgD[4,5]. To enable intravital two-photon microscopy of MZ B cells, we used transferred B cells from ubiquitin-green fluorescent protein (Ub-GFP)-expressing mice to *Cd19*-knockout (KO) mice that lack an endogenous MZ B cell population (Fig. 1a)[8]. After 8–12 weeks, the MZ was occupied by the transferred B cells, and the majority of the transferred GFP$^+$ B cells had a CD21^{hi}CD23^{lo} MZ B cell phenotype (Fig. 1b). Three hours before analysis, the mice were transfused with PKH26 (red) dye-labeled RBCs such that about 2% of RBCs in the recipient mice were labeled (Fig. 1c). The mice were also given transfers of CellTrace Violet (CTV)-labeled follicular B cells 1 or 2 d before to help identify lymphoid follicles. To guide expectations for the intravital imaging analysis, which can detect fluorescent cells at depths of up to 200 µm, thin sections were taken within 200 µm of the capsule and examined for the distribution of the transferred B cells and RBCs and for total IgD$^+$ follicular B cells. This analysis showed that occasional small follicular structures could be detected at this depth, and these had GFP$^+$ B cells superficially associated that were IgD^{lo} and thus were most likely MZ B cells (Fig. 1d). Clusters of large GFP-bright cells were also detected in the red pulp, distant from the B cell follicles, likely corresponding to plasma cells.

Scanning different regions of the spleen using intravital two-photon microscopy allowed for the identification of occasional areas with GFP$^+$ MZ B cells near clusters of CTV$^+$ follicular B cells (Fig. 1e and Supplementary Video 1). Labeled RBCs were observed passing near MZ B cells, and transient contacts between MZ B cells and RBCs could be detected (Fig. 1e and Supplementary Videos 2–4). Some RBCs encountered different MZ B cells during their movement (Fig. 1e and Supplementary Videos 2 and 3), and some MZ B cells were observed interacting with several RBCs (Supplementary Videos 2 and 4). In some regions of the MZ, the RBCs appeared to be moving in an irregular manner, perhaps within a turbulent and semiconfined space, whereas in other regions, the RBCs passed through the MZ with uniform flow (Supplementary Videos 2–4). Although we could readily detect RBC–MZ B cell contacts in each 20- to 30-min video, it is important to appreciate that only ~2% of the RBCs were labeled, and thus the contact frequency is expected to be 50-fold greater than imaged. These data establish that MZ B cells regularly contact RBCs in regions of flow within the MZ.

CD97 is required for MZ B cell homeostasis

Because frequent interactions were observed between RBCs and MZ B cells, we asked if there were ligand–receptor pairs expressed on the two cell types that might be required for MZ B cell function. Notable among the few surface molecules expressed by RBCs that engage surface receptors is CD55, the decay-accelerating factor of complement that is also a ligand for CD97 (encoded by *Adgre5*)[12,15]. Flow cytometric analysis showed that MZ B cells were marked by high CD97 expression (Fig. 2a,b). We therefore investigated the function of CD97 on MZ B cells. Analysis of CD97-deficient (*Adgre5*$^{-/-}$) mice (Extended Data Fig. 1a) revealed a significant reduction in MZ B cells (Fig. 2c,d). The frequencies of immature (T1 and T2) and mature follicular B cells were unaffected (Extended Data Fig. 1b). The frequency of B1 cells, another type of early-responder B cells[4], was also unaffected in the spleen (Extended Data Fig. 1c). Immunofluorescence staining of tissue sections for IgM and IgD showed a reduction in the thickness of the IgM^{hi} MZ in mice lacking CD97 (Fig. 2e and Extended Data Fig. 1d). Using mixed bone marrow (BM) chimeras, the CD97 requirement was established to be cell intrinsic (Fig. 2f and Extended Data Fig. 1e). Staining of tissue sections from IgH^a:IgH^b mixed BM chimeras showed a reduction in IgM^{hi} MZ thickness selectively in the CD97-deficient IgM^b MZ compartment (Extended Data Fig. 1f). By intravascular antibody labeling of blood-exposed spleen cells, about 55% of MZ B cells in wild-type (WT) mice were labeled; the remaining fraction was within follicles at the time of antibody injection and was protected from labeling[7] (Extended Data Fig. 1g). CD97 deficiency did not change the fraction of MZ B cells labeled, consistent with the notion that the rapid shuttling of MZ B cells between the MZ and follicle keeps the proportion of cells in each compartment intact even with the overall drop in MZ B cells (Fig. 2g). MZ B cells in littermate-matched control and *Cd97*-KO mice showed the same extent of turnover as determined by staining for the cell cycle antigen Ki-67 (Extended Data Fig. 1h) and the apoptosis marker Annexin V (Extended Data Fig. 1i).

We speculated that the reduced frequency of MZ B cells in CD97-deficient mice might be a consequence of loss into blood circulation. However, the frequency of MZ B cells in *Cd97*-KO blood was too low to detect reliably. We considered the possibility that there might be loss of very small numbers of cells at any given moment that could amount to a large loss over periods of days. We therefore asked whether conditional blockade of CD97 ligand binding could lead to a more synchronized release of cells. Indeed, when mice were treated with a CD97-blocking antibody, a small population of MZ B cells could be detected in the blood 3 h later (Fig. 2h). At this time point, the treatment was not sufficient to measurably deplete MZ B cells from the spleen (Extended Data Fig. 2a). However, more prolonged treatment with CD97-blocking antibody led to a reduction in MZ B cells, consistent with gradual loss from the spleen (Fig. 2i). A slight increase in follicular B cell frequency was observed (Extended Data Fig. 2b), likely due to the reduction in MZ B cells.

Intravital two-photon microscopy of the splenic red pulp in mice that harbored GFP$^+$ MZ B cells and PKH26$^+$ RBCs revealed large numbers of labeled RBCs passing through the red pulp, some at high speed within vessels or sinuses and others more slowly that were likely traveling through the parenchyma (Supplementary Videos 5 and 6). We noted occasional GFP$^+$ cells, possibly MZ B cells in the red pulp, in addition to

https://doi.org/10.1038/s41590-023-01690-z

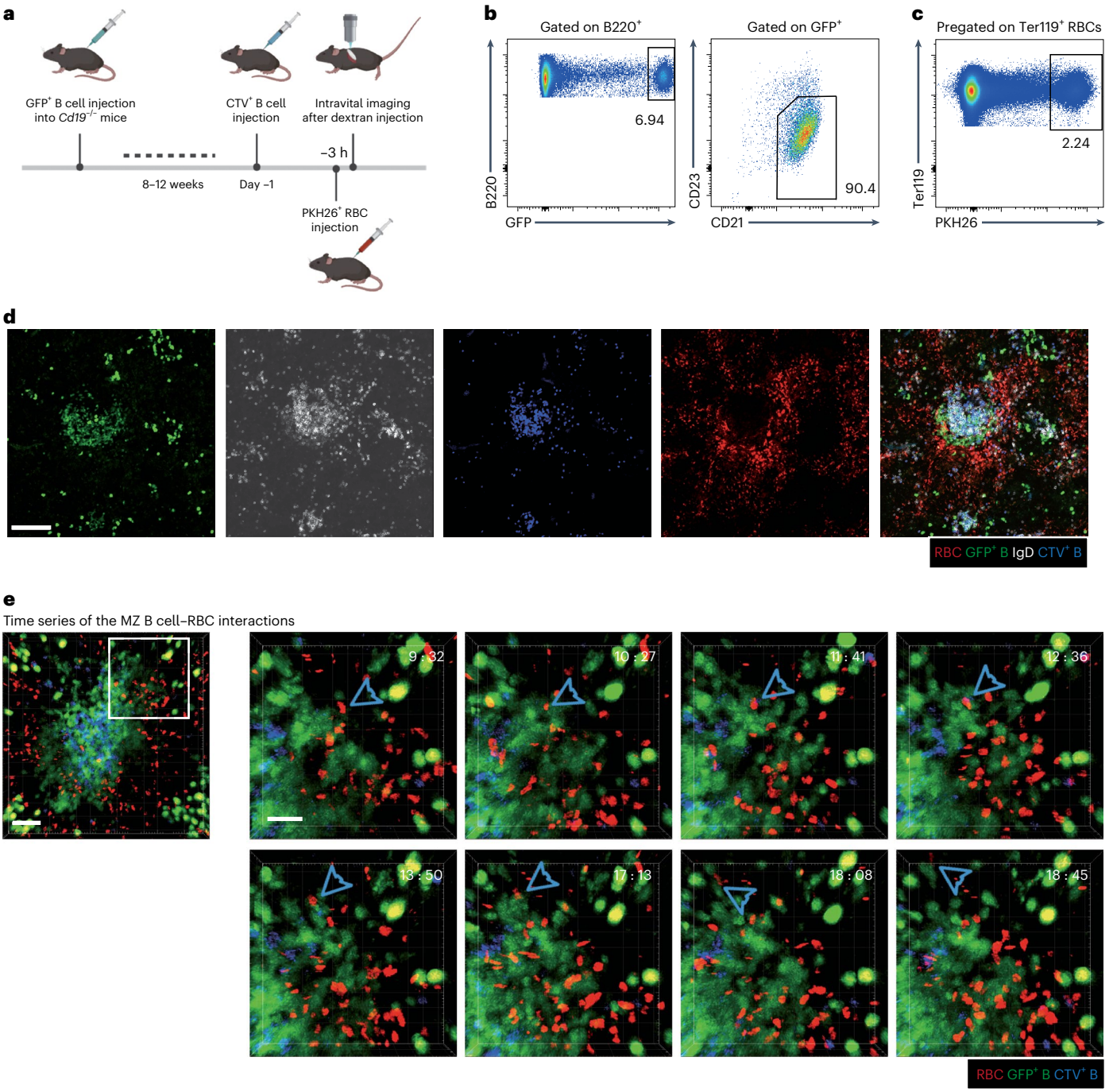

Fig. 1 | Intravital imaging reveals transient contacts between MZ B cells and RBCs. The behaviors of MZ B cells were observed with intravital two-photon microscopy in *Cd19*$^{-/-}$ mice reconstituted with Ub-GFP^{+} B cells. CTV-labeled naive B cells were used to identify follicles. PKH26-labeled RBCs were intravenously injected 3 h before imaging, and 70-kD Texas Red dextran was introduced 30 min before imaging. **a**, Schematic diagram of the intravital imaging protocol. **b**, Representative flow cytometry profiles of MZ B cells among GFP^{+} B cells 8–12 weeks after reconstitution. **c**, A representative flow cytometry profile of PKH26-labeled RBCs in total splenic RBCs. **d**, Representative distribution patterns of PKH26-labeled RBCs (red), GFP^{+} B cells (green), CTV-labeled B cells (blue) and IgD^{+} B cells (white) in the spleen; scale bar, 100 µm. The section shown is representative of multiple cross-sections from at least three mice. **e**, Examples of contacts between RBCs and MZ B cells (blue arrowhead) in spleens. The region (120 µm × 120 µm) indicated with white box (left; scale bar, 40 µm) was zoomed in for the time series (right; scale bar, 20 µm). One RBC was tracked interacting with several different MZ B cells. The interaction starts at 9:32 and ends at 18:45. Time is indicated in minutes:seconds. See corresponding Supplementary Videos 2–4. Data are representative of five independent experiments.

the large GFP^{hi} cells that are likely plasma cells (Supplementary Videos 5 and 6). While imaging spleens of mice that had been reconstituted with either WT or *Cd97*-KO Ub-GFP^{+} B cells, we noted occasional GFP^{+} *Cd97*-KO B cells being released into circulation (Fig. 2j and Supplementary Video 6). Although the trend for release of more *Cd97*-KO cells than WT cells did not reach statistical significance, this observation is consistent with the increased flow cytometric detection of MZ B cells in the blood after CD97 blockade. Integrin expression was intact in CD97-deficient mice and in WT mice after antibody blockade (Extended Data Fig. 2c–f).

To assess the fate of MZ B cells that have been released into blood circulation, we tracked GFP$^+$ MZ B cells in the first 18 h after intravenous transfer of splenocytes. Compared to the total number of MZ B cells that were injected, most cells were lost from the blood within 10 min, and only ~0.25% could be recovered 1 h later (Extended Data Fig. 2g,h). Somewhat greater numbers were present in the recipient spleen at this time, and a gradual increase in number occurred, reaching a plateau by 6 h that corresponded to a recovery of about 5% of the transferred MZ B cells. Transferred GFP$^+$ CD97-deficient MZ B cells showed a similar loss from circulation and similar initial appearance in the spleen, but these cells were not maintained and had largely decayed by 18 h (Extended Data Fig. 2i,j). Thus, a reduced ability to reseed the spleen may contribute to the overall splenic MZ B cell deficiency in CD97-deficient mice.

CD97-tethered ligand requirement in MZ B cells

We next characterized what features of CD97 were required for its in vivo function in MZ B cells. CD97 is composed of noncovalently attached NTF and CTF (Fig. 2a). Mutation of T419, the residue immediately following the GPS site, to glycine (T419G) prevents CD97 autoproteolysis but permits normal surface expression[21]. Using a *Cd97*-KO BM retroviral transduction and reconstitution approach, WT CD97 was able to restore MZ B cell accumulation, whereas the non-cleaved T419G mutant did not (Fig. 2k) despite comparable expression (Extended Data Fig. 2k). In these experiments, the transduced CD45.2$^+$ cells were detected using a Thy1.1 reporter; untransduced CD45.2$^+$ cells in the same BM chimeras were identified as Thy1.1$^-$ cells. The first ~10 amino acids following the GPS (Fig. 2a) are thought to function as a tethered ligand in CD97 and many other adhesion GPCRs[12,13]. In a cell line study, mutation of tethered ligand residue L424 to alanine (L424A) or M425 to lysine (M425K) reduced CD97 signaling in vitro[22]. When *Cd97*-KO mice were reconstituted with BM transduced with CD97 L424A or M425K, the MZ B cell compartment was not rescued (Fig. 2k) despite surface expression being comparable to that observed in WT mice (Extended Data Fig. 2k). CD97 has a C-terminal motif that can interact with PDZ domain proteins[21]. CD97 with a mutation in this PDZ-binding motif (PBM) had intact expression (Extended Data Fig. 2k) and was functional in restoring MZ B cells, although perhaps less efficiently than WT CD97 (Fig. 2k). Taken together, these data are consistent with a model where extraction of the CD97 NTF leads to activation of the receptor by a tethered ligand, and this signal promotes MZ B cell retention and homeostasis in the spleen.

CD97 in MZ B cells signals via $G\alpha_{13}$ and ARHGEF1

Because prior studies in cell lines and type 2 conventional dendritic cells indicated that CD97 can signal via $G\alpha_{13}$-containing heterotrimeric G proteins[17,21,23,24], and other work showed a role for $G\alpha_{12}/G\alpha_{13}$ in MZ B cells[25], we asked if $G\alpha_{13}$ may be required for CD97 function in MZ B cells. Like CD97-deficient mice, animals lacking $G\alpha_{13}$ selectively in B cells (*Gna13*$^{fl/fl}$ Mb1-Cre$^+$ conditional knockout (cKO), labeled as *Gna13*^{cKO}) showed a twofold reduction in MZ B cell frequency (Fig. 3a,b). There was no effect of $G\alpha_{13}$ deficiency on immature or mature B cell frequencies in the spleen (Extended Data Fig. 3a). Splenic B1 cells were also unaffected (Extended Data Fig. 3b). Microscopy showed that *Gna13*^{cKO} mice had reduced MZ thickness (Fig. 3c and Extended Data Fig. 3c). Using mixed BM chimeras, the $G\alpha_{13}$ requirement for MZ B cell homeostasis was confirmed to be cell intrinsic (Fig. 3d). Importantly, chronic anti-CD97 treatment of $G\alpha_{13}$-deficient mice did not cause any further reduction in MZ B cell frequencies, whereas it did reduce the MZ B cell compartment in WT mice, as expected (Fig. 3e). $G\alpha_{12}$ deficiency did not affect MZ B cell frequencies (Extended Data Fig. 3d,e). These data confirm that CD97 and $G\alpha_{13}$ function in the same pathway. ARHGEF1 (also known as p115RhoGEF or Lsc) is a Rho-activating guanidine nucleotide exchange factor and the best-defined effector of $G\alpha_{13}$ (ref. 26). A similar series of experiments performed with ARHGEF1-deficient mice showed that this $G\alpha_{13}$ effector is needed for MZ B cell homeostasis (Fig. 3f–h and Extended Data Fig. 3f), in agreement with a prior study[27]. ARHGEF1 deficiency did not affect immature B cell or B1 cell frequencies in the spleen, and it led to a slight increase in follicular B cell frequencies (Extended Data Fig. 3g,h). Mixed BM chimeras established that ARHGEF1 acts in a cell-intrinsic manner in MZ B cells (Fig. 3i). These findings are in agreement with CD97 signaling via $G\alpha_{13}$ and ARHGEF1 in MZ B cells.

CD55 on RBCs acts as the CD97 ligand

CD55 is well expressed on RBCs and is also present on various other hematopoietic cells[15,17]. Interestingly, MZ B cells expressed low amounts of CD55 compared to follicular B cells (Fig. 4a), perhaps ensuring limited *cis* interaction between CD55 and CD97 and maximal availability to interact with CD55 on other cells. To test the importance of CD55 for CD97-dependent functions in MZ B cells, we analyzed *Cd55*$^{-/-}$ mice. MZ B cell frequencies were reduced in *Cd55*$^{-/-}$ mice to a similar extent as in *Cd97*-KO mice, and the MZ showed a similar decrease in thickness in imaging (Fig. 4b–d and Extended Data Fig. 4a). Immature, follicular and B1 cell frequencies in the spleen were unaltered by CD55 deficiency (Extended Data Fig. 4b,c). The fractions of MZ B cells in the cell cycle based on Ki-67 staining (Extended Data Fig. 4d) or that were undergoing cell death based on Annexin V staining (Extended Data Fig. 4e) were not changed by CD55 deficiency. Mixed BM chimeras showed that CD55 was not required intrinsically by MZ B cells (Fig. 4e). Importantly, when cells lacked both CD55 and CD97 (double KO (dKO)), the deficiency in MZ B cells was of the same magnitude as for single-KO cells (Fig. 4f), consistent with these genes acting in the same pathway and with CD55 serving as the only CD97 ligand involved in MZ B cell maintenance.

In addition to being expressed by RBCs and some other hematopoietic cells, CD55 is expressed by various non-hematopoietic cells[17,28]. As a broad approach to determine the necessary CD55-expressing cell types for MZ B cell homeostasis, we generated reciprocal BM chimeras. In mice lacking CD55 in all radiation-sensitive BM-derived cells, there was a deficiency in MZ B cells (Extended Data Fig. 4f), whereas in mice lacking CD55 in radiation-resistant cells, including all stromal cells, the MZ B cell compartment remained intact (Extended Data Fig. 4g).

Fig. 2 | CD97 is required for MZ B cell homeostasis. a, Structural components of CD97. Triangles indicate EGF domains. The ten amino acids (419–428) following the GPS are indicated. **b**, Representative histogram plot of CD97 on MZ and follicular (FO) B cells; ISO, isotype control. **c**,**d**, Flow cytometry profiles (**c**) and frequencies of MZ B cells in B cells (**d**; left) and total splenocytes (**d**; right) in *Adgre5*$^{-/-}$ ($n = 16$) and control ($n = 14$) mice. **e**, Distribution of IgM^{hi} MZ (red) and IgD^{hi} follicular (blue) B cells in indicated spleens; scale bar, 200 µm. Sections are representative of multiple cross-sections from at least three mice of each type. **f**, Flow cytometry profiles (left) and frequencies (right) of MZ B cells of the indicated genotypes in WT:*Adgre5*$^{-/-}$ ($n = 9$) and control ($n = 9$) chimeras. **g**, Frequencies of in vivo anti-CD45-phycoerythrin (PE)-labeled MZ B cells of the indicated genotypes in WT:*Adgre5*$^{-/-}$ ($n = 8$) and control ($n = 8$) chimeras. Lines connect data from the same animals. **h**, Flow cytometry profiles (left) and frequencies (right) of MZ B cells in blood in WT mice 3 h after treatment with anti-CD97 ($n = 8$) or saline ($n = 8$). **i**, Frequencies of MZ B cells in the spleen in WT mice after 4 d of treatment with anti-CD97 ($n = 13$) or saline ($n = 12$). **j**, Frequencies of 'leaving cells' (GFP$^+$ B cells that enter large vessels) in mice reconstituted as in Fig. 1a with *Adgre5*$^{-/-}$ ($n = 10$) and *Adgre5*$^{+/+}$ ($n = 6$) MZ B cells. See corresponding Supplementary Videos 5 and 6. **k**, BM chimeras were reconstituted with 10% non-transduced CD45.1 WT and 90% CD45.2 *Adgre5*$^{+/+}$ or *Adgre5*$^{-/-}$ BM transduced with retroviral constructs encoding *Adgre5* WT ($n = 15$) or its mutants ($n = 8$ in L424A, $n = 5$ in M425K, $n = 10$ in PBM and $n = 8$ in T419G) or empty vector (CON; $n = 18$ in *Adgre5*$^{+/+}$ and $n = 20$ in *Adgre5*$^{-/-}$). The graph shows the frequencies of MZ B cells in Thy1.1$^+$ or Thy1.1$^-$ B cells. Data are pooled from four (**d** and **i**), two (**f**–**h**), five (**j**) or six (**k**) independent experiments. Each symbol represents one mouse, and lines denote means. Statistical significance was tested by two-tailed *t*-test (**d**, **h**, **i** and **j**) or two-way analysis of variance (ANOVA) followed by a Sidak's multiple-comparisons test (**f**, **g** and **k**).

https://doi.org/10.1038/s41590-023-01690-z

Although follicular B cells abundantly express CD55, analysis of 85:15 *Rag1*$^{-/-}$:*Cd55*$^{-/-}$ BM chimeras that lack CD55 on all B cells and most T cells revealed an intact MZ B cell compartment (Extended Data Fig. 4h–j). RBCs make up 99.9% of the cells in blood[29]. RBCs also express CD55, although at a lower surface level than B cells (Extended Data Fig. 4k). To test whether RBCs were the relevant source of CD55, WT or *Cd55*-KO RBCs were transferred into *Cd55*-KO mice. Because the MZ B cell compartment is slow to turn over[4], the transfusion was performed weekly for 4 weeks. At the end of the transfusion, approximately 65% of RBCs were of donor origin (Extended Data Fig. 4l). Reconstitution of *Cd55*$^{-/-}$ mice with WT, but not *Cd55*-KO, RBCs rescued the size of the MZ B cell compartment (Fig. 4g). Platelets also express CD55 (ref. 30). To test for a possible contribution of platelet CD55 to MZ B cell homeostasis, 85:15 mixed BM chimeras between *Mpl*$^{-/-}$ BM (unable to generate

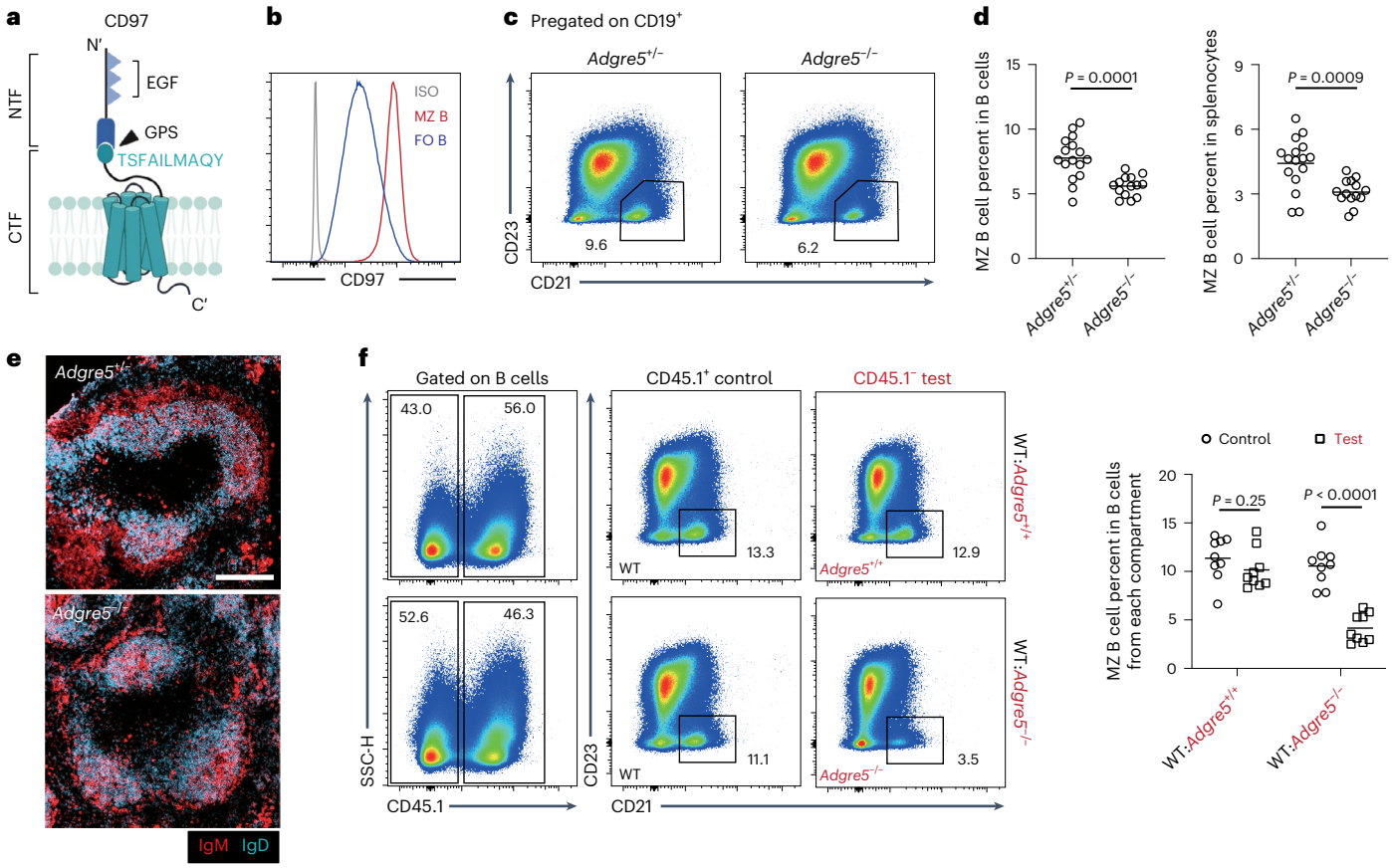

https://doi.org/10.1038/s41590-023-01690-z

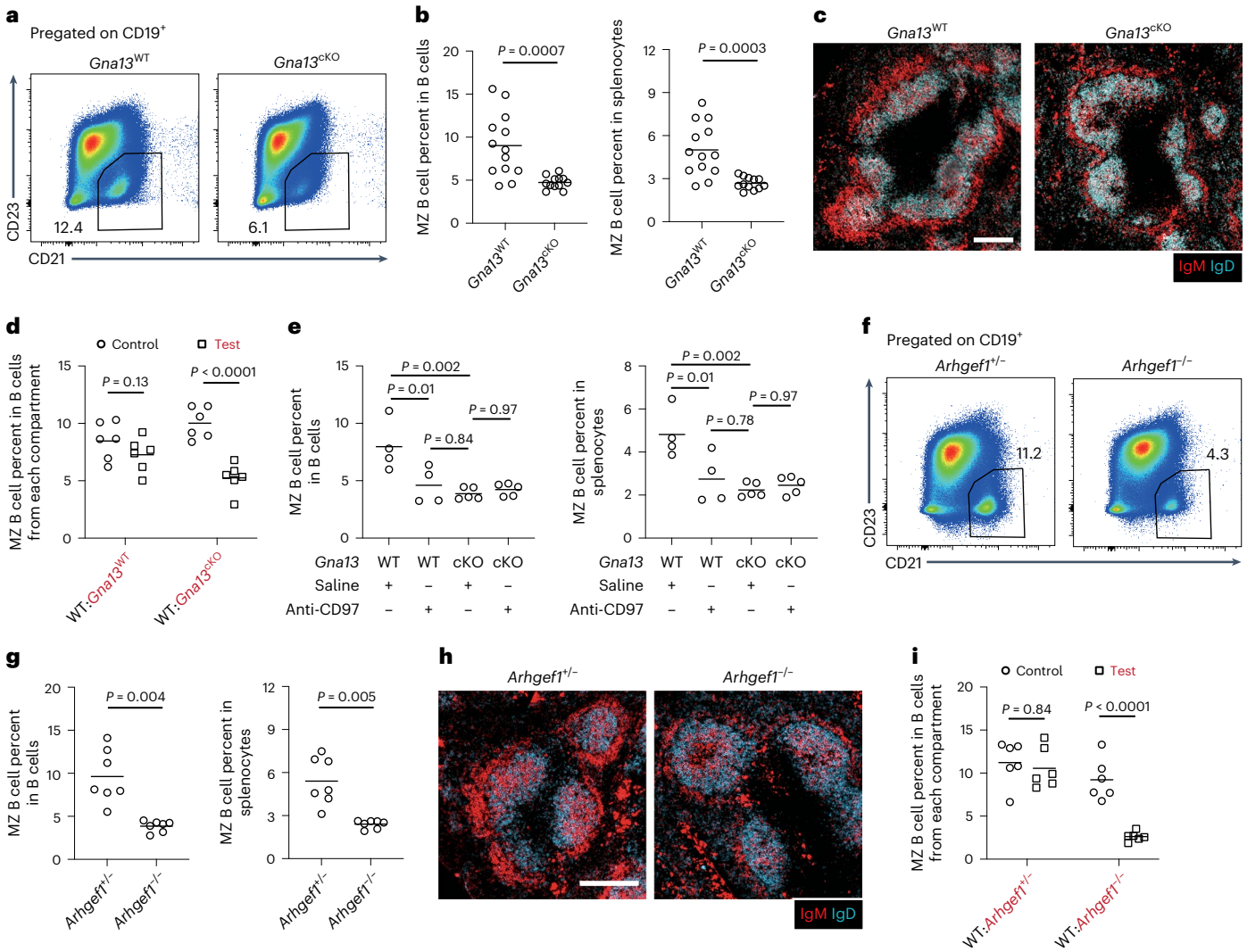

Fig. 3 | The $G\alpha_{13}$–ARHGEF1 signaling pathway is required in MZ B cells. **a**,**b**, Representative flow cytometry profiles (**a**) and frequencies of MZ B cells in total CD19$^+$ B cells (**b**; left) and in total splenocytes (**b**; right) in *Gna13*^{cKO} ($n = 12$) and control ($n = 13$) mice. **c**, Representative distribution patterns of IgM^{hi} MZ B cells (red) relative to IgD^{hi} follicular B cells (blue) in spleens of mice of the indicated genotypes; scale bar, 200 µm. **d**, Mixed (50:50) BM chimeras were made with CD45.1 WT and CD45.2 *Gna13*^{WT} or *Gna13*^{cKO} BM cells. Frequencies of MZ B cells among the indicated genotype CD19$^+$ B cells in WT:*Gna13*^{cKO} ($n = 6$) and control ($n = 6$) mixed BM chimeras. **e**, Frequencies of MZ B cells in total CD19$^+$ B cells (left) and in total splenocytes (right) in *Gna13*^{cKO} ($n = 5$) and control ($n = 4$) mice 4 d after treatment with anti-CD97 or saline. **f**,**g**, Representative flow cytometry profiles (**f**) and frequencies of MZ B cells in total CD19$^+$ B cells (**g**; left) and in total splenocytes (**g**; right) in *Arhgef1*$^{-/-}$ ($n = 7$) and control ($n = 7$) mice. **h**, Representative distribution patterns of IgM^{hi} MZ B cells (red) relative to IgD^{hi} follicular B cells (blue) in spleens of mice of the indicated genotypes; scale bar, 200 µm. **i**, Mixed (50:50) BM chimeras were made with CD45.1 WT and CD45.2 *Arhgef1*$^{+/-}$ or *Arhgef1*$^{-/-}$ BM cells. Frequencies of MZ B cells among the indicated genotype CD19$^+$ B cells in WT:*Arhgef1*$^{-/-}$ ($n = 6$) and control ($n = 6$) mixed BM chimeras. Data are pooled from four (**b**) or two (**d**, **e**, **g** and **i**) independent experiments. Sections are representative of multiple cross-sections from at least three mice of each type (**c** and **h**). Each symbol represents one mouse, and lines denote means. Statistical significance was tested by two-tailed *t*-test (**b** and **g**) or two-way ANOVA followed by a Sidak's multiple-comparisons test (**d** and **i**) or one-way ANOVA followed by a Tukey's multiple-comparisons test (**e**).

platelets) and *Cd55*$^{-/-}$ BM were made such that all the platelets in these mice were CD55 deficient (Fig. 4h). CD55 deficiency on platelets did not lead to a reduction in the MZ B cell compartment (Fig. 4i). Thus, RBCs are the key CD55$^+$ cell type needed for MZ B cell homeostasis.

CD55-dependent extraction of the CD97 NTF under shear stress

Flow cytometric analysis of MZ B cells for CD97 showed that surface levels were elevated in mice lacking CD55 (Fig. 5a) and returned to normal in mice receiving transfers of RBCs from WT donor mice (Fig. 5a). Under in vitro conditions, MZ B cell CD97 surface abundance was reduced after 45 min of co-incubation with WT RBCs in a shaker at 1,000 r.p.m., which generates a shear stress of approximately 14 dyne cm^{-2} (ref. 31; Fig. 5b). MZ B cells incubated with RBCs without shaking or incubated with *Cd55*$^{-/-}$ RBCs with shaking did not show any reduction in CD97 surface abundance (Fig. 5b). When MZ B cells were taken from CD97-deficient mice that had been reconstituted with BM transduced with a construct encoding the non-cleavable T419G form of CD97, incubation with RBCs with shaking did not lead to any change in CD97 surface abundance, consistent with the reduced expression being due to extraction of the NTF (Fig. 5c). To confirm that exposure to CD55$^+$ RBCs under shear stress was causing NTF extraction and not CD97 degradation, we used MZ B cells from chimeras that had been reconstituted with a CD97–GFP fusion protein (Extended Data Fig. 5a). Exposure of MZ B cells expressing this construct to *Cd55*$^{+/+}$ RBCs under shear stress conditions led to reduced CD97 surface staining but had no effect on GFP intensity (Extended Data Fig. 5b,c), confirming that the reduced staining was

https://doi.org/10.1038/s41590-023-01690-z

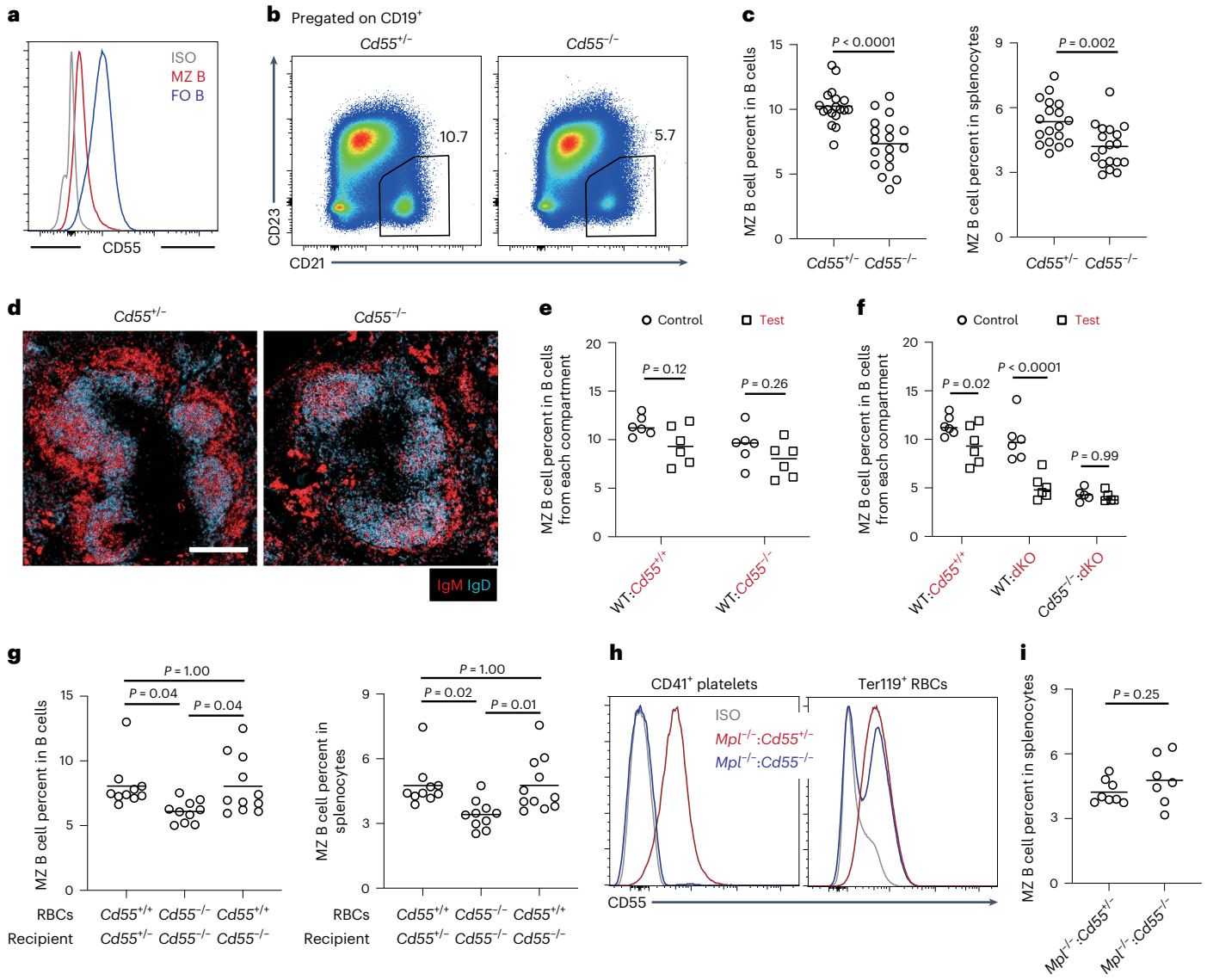

Fig. 4 | CD55 on RBCs is required for MZ B cell maintenance. a, Representative histogram plot of surface CD55 on MZ B cells and follicular B cells. **b**,**c**, Representative flow cytometry profiles (**b**) and frequencies of MZ B cells in total CD19$^+$ B cells (**c**; left) and in total splenocytes (**c**; right) in *Cd55*$^{-/-}$ ($n = 18$) and control ($n = 18$) mice. **d**, Representative distribution patterns of IgM^{hi} MZ B cells (red) relative to IgD^{hi} follicular B cells (blue) in spleens of mice of the indicated genotypes; scale bar, 200 µm. Sections are representative of multiple cross-sections from at least three mice of each type. **e**, Mixed (50:50) BM chimeras were made with CD45.1 WT and CD45.2 *Cd55*$^{+/+}$ or *Cd55*$^{-/-}$ BM cells. Frequencies of MZ B cells of the indicated genotype CD19$^+$ B cells in WT:*Cd55*$^{-/-}$ ($n = 6$) and control ($n = 6$) mixed BM chimeras. **f**, Mixed (50:50) BM chimeras were made with CD45.1 WT and CD45.2 WT ($n = 6$), *Adgre5*$^{-/-}$*Cd55*$^{-/-}$ (dKO; $n = 6$) or *Cd55*$^{-/-}$ and dKO ($n = 5$) BM cells. Frequencies of MZ B cells among the indicated genotype CD19$^+$ B cells in mixed BM chimeras. **g**, RBC transfusions were performed from *Cd55*$^{-/-}$ or *Cd55*$^{+/+}$ mice to the indicated recipient mice once per week, and analysis was performed after 4 weeks. Frequencies of MZ B cells in total B cells (left) and in total splenocytes (right) in mice with purified RBCs transfused as indicated ($n = 10$ or 11 recipients in each group) are shown. **h**,**i**, Mixed chimeras were made with 85% *Mpl*$^{-/-}$ and 15% *Cd55*$^{+/+}$ or *Cd55*$^{-/-}$ BM cells. A representative histogram shows surface CD55 on platelets (left) and RBCs (right) in chimeras (**h**). Frequencies of MZ B cells in total splenocytes in *Mpl*$^{-/-}$:*Cd55*$^{-/-}$ ($n = 7$) and control ($n = 8$) chimeras are shown (**i**). Data are pooled from five (**c**), two (**e**, **f** and **i**) or three (**g**) independent experiments. Each symbol represents one mouse, and lines denote means. Statistical significance was tested by two-tailed *t*-test (**c** and **i**) or two-way ANOVA followed by Sidak's multiple-comparisons test (**e** and **f**) or one-way ANOVA followed by Tukey's multiple-comparisons test (**g**).

due to extraction of the NTF. Finally, we transferred splenic B cells from chimeras expressing the CD97–GFP fusion protein into WT or *Cd55*-KO recipients and analyzed the transferred cells in recipient blood 30 min later. Due to the rarity of transferred MZ B cells in the recipient blood, we instead tracked changes in CD97 and GFP abundance in transferred follicular B cells. Compared to B cells in *Cd55*-KO recipients, B cells in the blood of WT recipients had low CD97 surface staining, but GFP intensity was unaffected (Fig. 5d,e). Taken together, these data provide evidence that CD97 on MZ B cells undergoes NTF extraction following encounter with CD55$^+$ RBCs under shear stress conditions.

Human splenic MZ B cells are CD27^{hi}, and they have variable levels of CD1c[32,33]. Analysis of published single-cell RNA-sequencing data of human spleen B cells showed higher *ADGRE5* mRNA expression in the two MZ B cell clusters, although expression of transcripts did not appear abundant compared to that for CD27 or CR2 (Extended Data Fig. 5d)[33]. However, fluorescence-activated cell sorting analysis established that most MZ B cells express higher amounts of CD97 protein than follicular B cells (Fig. 5f and Extended Data Fig. 5e). Human RBCs were positive for CD55 expression (Extended Data Fig. 5f), as expected[30]. When RBC-depleted human splenocytes were incubated

https://doi.org/10.1038/s41590-023-01690-z

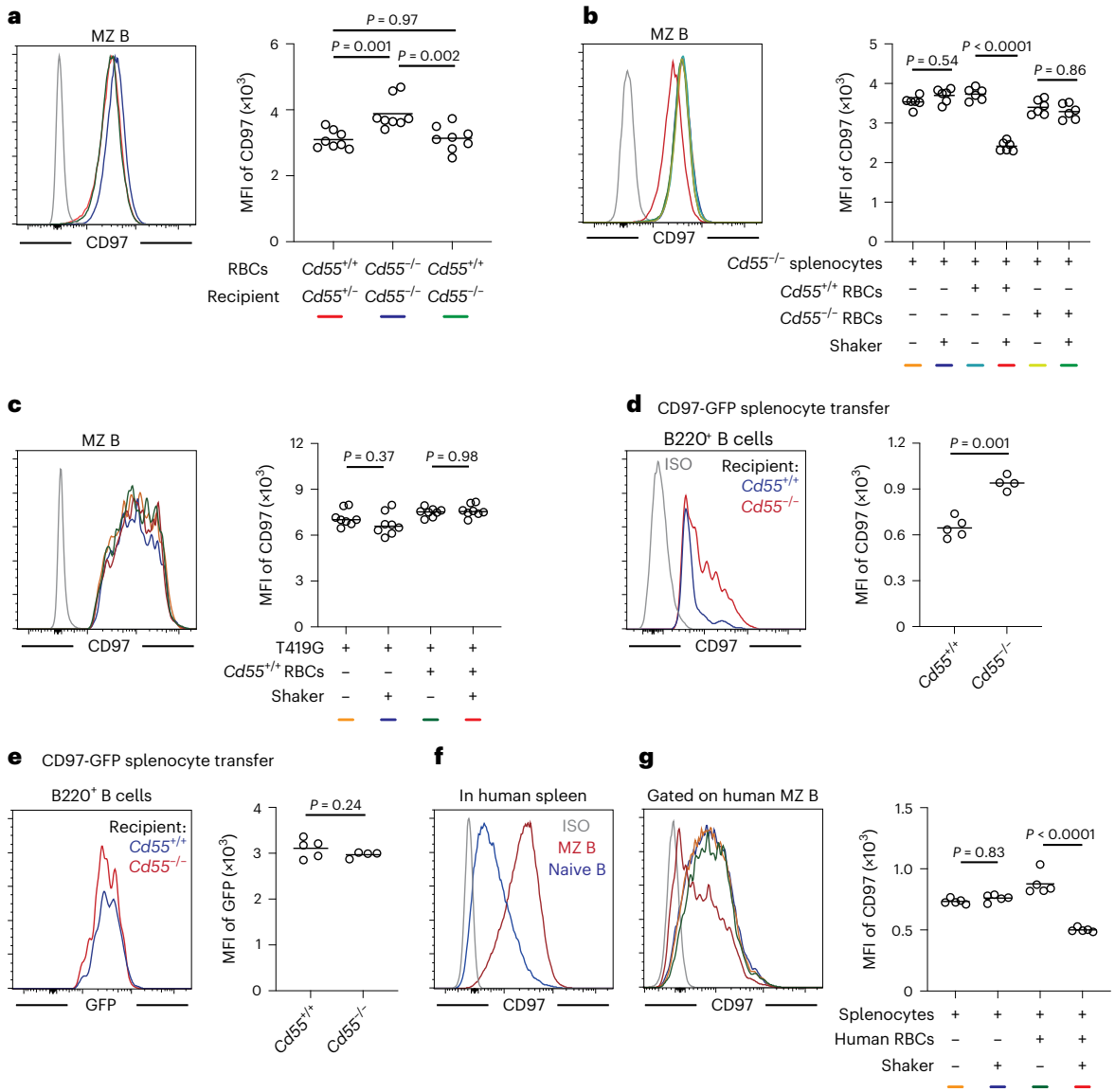

Fig. 5 | CD55-mediated CD97 NTF extraction is dependent on shear stress and is conserved in human MZ B cells. a, Representative histogram (left) and geometric mean fluorescence intensity (MFI; right) of surface CD97 expression on MZ B cells in mice with blood transfusion as indicated ($n = 8$ recipients in each group). Line colors in the histogram are for mice of the types shown by color code beneath the graph. **b**,**c**, Splenocytes from *Cd55*$^{-/-}$ mice (**b**; $n = 6$ in each group) or CD97 T419G-expressing BM chimeras (**c**; $n = 8$ in each group) were cocultured for 45 min with *Cd55*$^{-/-}$ or *Cd55*$^{+/+}$ RBCs on a shaker or not. Representative histograms (left) and MFIs (right) of surface CD97 expression on MZ B cells are shown. Line colors in the histograms are for conditions of the types shown by color codes beneath the graphs. Each symbol represents one incubation, and each donor contributes two incubations. **d**,**e**, MFI of surface CD97 expression (**d**) and GFP (**e**) on transferred MZ B cells from CD97–GFP fusion protein-expressing BM chimeras in blood collected from *Cd55*$^{-/-}$ ($n = 4$) or *Cd55*$^{+/+}$ ($n = 5$) recipients after a 30-min transfer as indicated. Each symbol represents one mouse. **f**, Representative histogram plot of surface CD97 on naive B cells and MZ B cells from the human spleen. **g**, Representative histogram (left) and MFI (right) of surface CD97 expression on human MZ B cells after incubation for 45 min with human RBCs on a shaker or not ($n = 5$ in each group). Each symbol represents one incubation, and line colors in the histogram are for conditions of the types shown by color code beneath the graph. Lines in graph denote means. Data are pooled from two independent experiments (**a**–**e**) or are representative of two independent experiments (**g**). Statistical significance was tested by one-way ANOVA followed by Tukey's multiple-comparisons test (**a**–**c** and **g**) or two-tailed *t*-test (**d** and **e**).

in the presence of human RBCs under shear stress, there was a marked reduction in CD97 surface staining compared to splenocytes incubated without RBCs or without shear stress (Fig. 5g). These data suggest that human MZ B cells experience CD97 NTF extraction during interactions with RBCs under shear stress conditions.

CD97 promotes cell membrane retraction

Activation of Rho-based signaling is established to promote retraction of cell membrane processes, and there is in vitro evidence of CD97 activation of Rho[21,23,34]. However, it remains unclear whether shear stress-mediated activation of CD97 is sufficient to engage Rho activity and membrane retraction. We examined the impact of CD97 expression (Extended Data Fig. 6a) on the morphology of adherent HEK293T cells. Cells expressing WT CD97 or the cleavage-resistant T419G CD97 variant showed a similar irregular morphology (Extended Data Fig. 6b). By contrast, cells expressing the CD97 CTF were more rounded (Extended Data Fig. 6b). The differences in shape were confirmed by comparing the longest dimension of the cells under each condition (Fig. 6a and Extended Data Fig. 6c).

https://doi.org/10.1038/s41590-023-01690-z

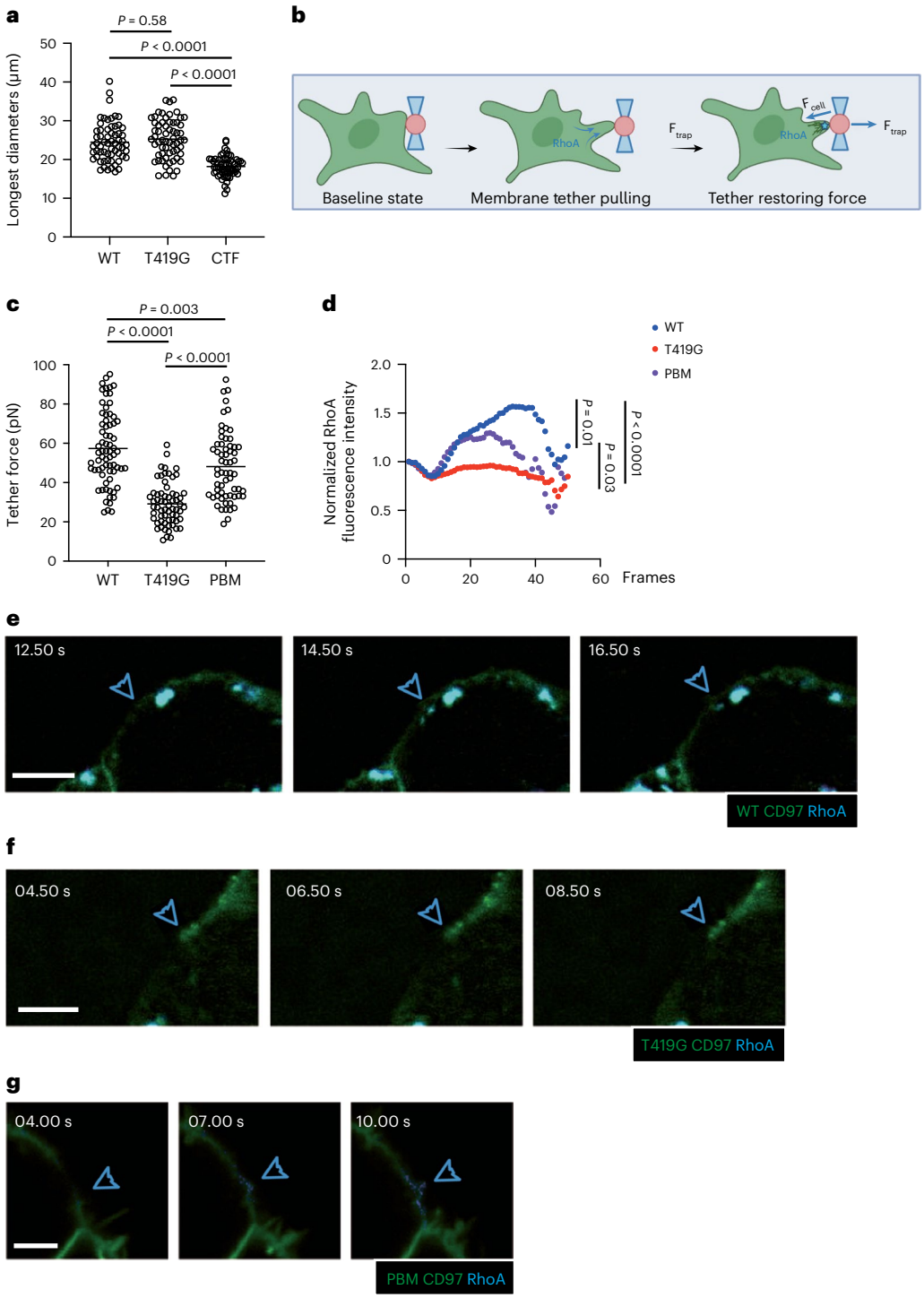

Fig. 6 | CD97 promotes cell membrane retraction through activation of RhoA. **a**, HEK293T cells were transfected with CD97 (WT)–GFP, CD97 (T419G)–GFP or CTF–GFP fusion constructs. Longest diameters of individual WT- ($n = 62$), T419G- ($n = 62$) and CTF-transfected ($n = 63$) cells are shown. Each symbol represents one cell. One of three independent experiments with similar results is shown. **b**, Schematic diagram of an optically trapped ligand-coated bead applying pulling force while in contact with the cell membrane. The cell is also indicated to contain an anillin–GFP RhoA biosensor. **c**,**d**, HEK293T cells were cotransduced with anillin–GFP RhoA biosensor and CD97 (WT)–Scarlet, CD97 (T419G)–Scarlet or CD97 (PBM)–Scarlet fusion lentivirus and sorted. **c**, Cell trap forces of individual WT- ($n = 70$), T419G- ($n = 64$) and PBM-transduced ($n = 62$) cells. **d**, Normalized active RhoA biosensor fluorescence intensity of WT- ($n = 27$), T419G- ($n = 20$) and PBM-transduced ($n = 32$) cells as indicated. **e**–**g**, Examples of anillin–GFP active RhoA biosensor signals at the site of bead contact and membrane tether (blue arrowhead) of one HEK293T cell expressing CD97 (WT)–GFP fusion (**e**), CD97 (T419G)–GFP fusion (**f**) or CD97 (PBM)–GFP fusion (**g**) protein. The blue arrowhead indicates the site of bead pulling. The time series begins at the start time for pulling, which was about 30 s after the bead contacted the cell. See corresponding Supplementary Videos 7–12; scale bar, 5 μm (**e** and **f**); scale bar, 3 μm (**g**). Data are representative of three independent experiments (**a**) or a pool from two (**c**–**g**) independent experiments. Statistical significance was tested by one-way ANOVA followed by a Tukey's multiple-comparisons test (**a** and **c**) or mixed-effects analysis followed by a Geisser–Greenhouse correction (**d**).

https://doi.org/10.1038/s41590-023-01690-z

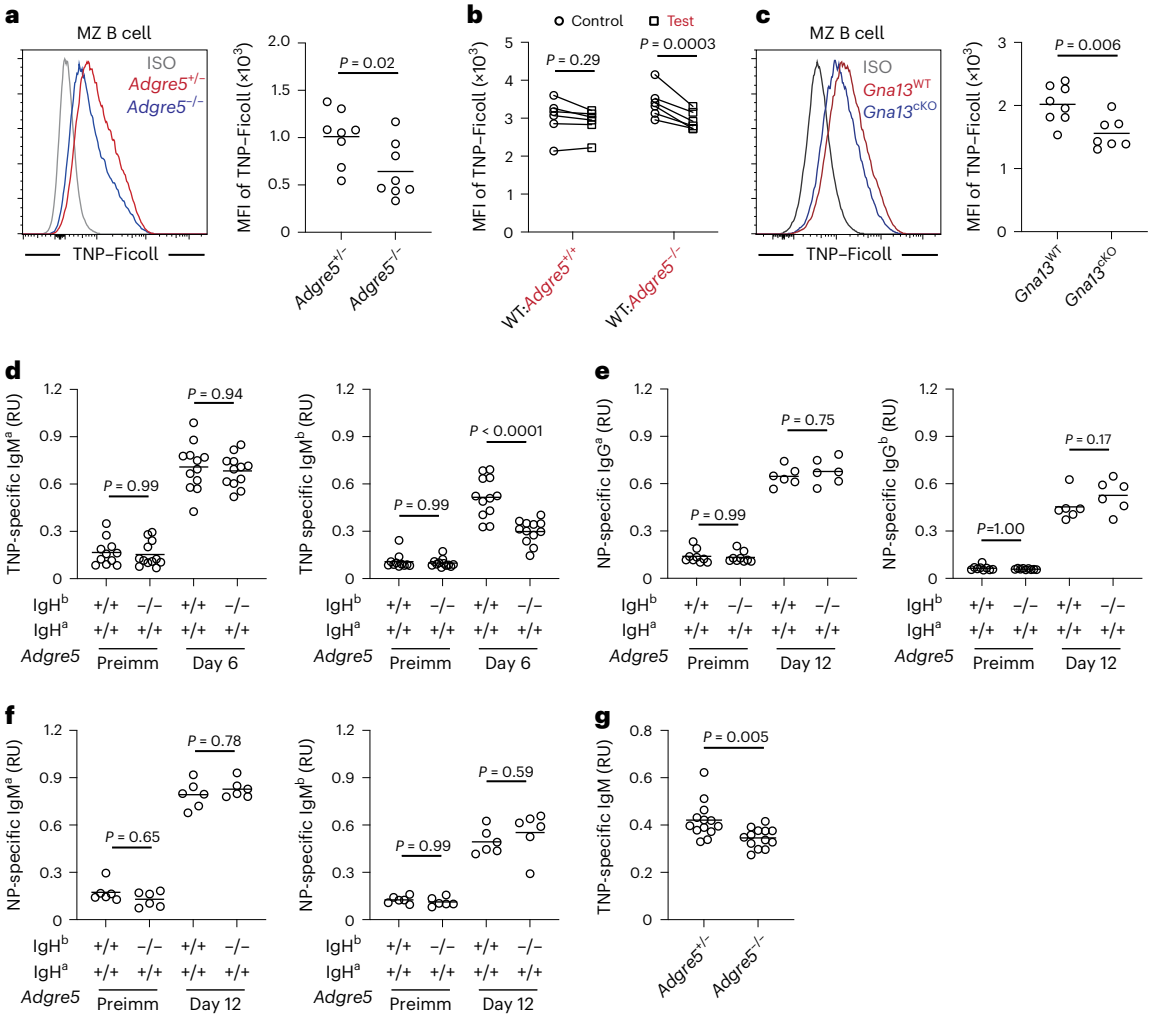

Fig. 7 | CD97 deficiency leads to defective antibody responses to T cell-independent antigen. a–**c**, Mice were analyzed 40 min after intravenous TNP–Ficoll injection. **a**, Representative histogram (left) and MFI (right) of TNP–Ficoll levels on MZ B cells in *Adgre5*$^{-/-}$ ($n = 8$) and control ($n = 8$) mice. **b**, MFI of TNP–Ficoll levels on MZ B cells in WT:*Adgre5*$^{-/-}$ ($n = 6$) and control ($n = 6$) mixed BM chimeras. Lines connect data from the same animals. **c**, Representative histogram (left) and MFI (right) of TNP–Ficoll levels on MZ B cells in *Gna13*^{cKO} ($n = 8$) and control ($n = 7$) mice. **d**–**f**, Enzyme-linked immunosorbent assay (ELISA) analysis of serum from 50:50 mixed IgH^a WT (*Adgre5*$^{+/+}$) with IgH^b *Adgre5*$^{+/+}$ or *Adgre5*$^{-/-}$ chimeras. **d**, Mixed chimeras were immunized intravenously with TNP–Ficoll. TNP-specific IgM^a (left) and IgM^b (right) in serum from the indicated time points ($n = 11$ or 12 chimeras for each condition). **e**,**f**, Mixed chimeras were immunized intraperitoneally with NP-CGG with Alum. NP-specific IgG1^a (**e**; left), IgG1^b (**e**; right; $n = 9$ for preimmunized (preimm) and $n = 6$ for postimmunized groups), IgM^a (**f**; left) and IgM^b (**f**; right; $n = 6$ for each group) in serum from the indicated time points. **g**, TNP-specific IgM in serum from *Adgre5*$^{+/-}$ ($n = 13$) or *Adgre5*$^{-/-}$ ($n = 13$) mice day 5 after TNP–Ficoll immunization. In **d**–**g**, RU indicates relative units. Data are pooled from two (**a**–**c**, **e** and **f**) or three (**d** and **g**) independent experiments. Each symbol represents one mouse, and lines denote means. Statistical significance was tested by two-tailed *t*-test (**a**, **c** and **g**) or two-way ANOVA followed by a Sidak's multiple-comparisons test (**b**) or one-way ANOVA followed by a Tukey's multiple-comparisons test (**d**–**f**).

To directly test whether the CD55–CD97 interaction leads to membrane retraction, we turned to optical tweezers[35]. Beads coated with recombinant mouse CD55 were brought into contact with HEK293T cells expressing mouse CD97–Scarlet for 30 s to allow a membrane tether attachment. Subsequently, the bead was pulled away using the optical trap[35]. The displaced bead remains attached to the cell via a membrane tether, which exerts a restoring force that is proportional to the square of membrane tension[35,36] (Fig. 6b). These measurements revealed that cells expressing WT CD97 exerted an almost twofold greater tether force than cells expressing the signaling defective T419G CD97 variant (Fig. 6c and Extended Data Fig. 6d). Similar analysis of the CD97 PBM variant mutated in the C-terminal PBM showed a partial reduction in the retraction response (Fig. 6c and Extended Data Fig. 6d). Using cells that also expressed the active RhoA biosensor anillin[37] and WT CD97, induction of RhoA activation at the bead contact site was observed within a few seconds after applying a pulling force on the bead (Fig. 6d,e and Supplementary Videos 7 and 8). RhoA activation was not observed at the bead contact site in equivalently treated cells that expressed the T419G CD97 mutant (Fig. 6d,f and Supplementary Videos 9 and 10). RhoA activation was induced by the CD97 PBM mutant, although the activity was less sustained than for WT CD97, suggesting that there is a difference in the kinetics of recruitment and activation of RhoA (Fig. 6d,g and Supplementary Videos 11 and 12). These data are consistent with CD97 becoming activated to signal via RhoA and cause membrane retraction after binding CD55$^+$ particles and exposure to pulling forces.

CD97 deficiency leads to reduced T cell-independent responses

MZ B cells have an established role in mounting rapid antibody responses against circulating T cell-independent antigens, such as bacterial capsular polysaccharides[4]. Trinitrophenol (TNP)-haptenated Ficoll, a large highly branched polysaccharide, is widely used as a model

T cell-independent antigen. Like other polysaccharide antigens, Ficoll becomes rapidly coated with complement fragments following systemic injection, and the complex can bind to MZ B cells via complement receptors[38,39]. Forty minutes after injection, the amount of TNP–Ficoll bound to MZ B cells was lower in *Cd97*-KO mice than in littermate control mice (Fig. 7a). This defect was cell intrinsic, as *Cd97*-KO MZ B cells bound less TNP–Ficoll than WT B cells in mixed BM chimeras (Fig. 7b). Similar findings were made in mice lacking $G\alpha_{13}$ in B cells (Fig. 7c). CD55-deficient and ARHGEF1-deficient mice also showed reductions in TNP–Ficoll capture (Extended Data Fig. 7a–c). These data indicate that the MZ B cells remaining in CD97 pathway-deficient mice are altered in their ability to capture a blood-borne antigen. When spleen B cells were injected intravenously just before treating mice with TNP–Ficoll, WT and *Cd97*-KO MZ B cells in blood circulation captured Ficoll with similar efficiency (Extended Data Fig. 7d). B1 cells can also contribute to T cell-independent antibody responses[5]. However, peritoneal B1 cells showed minimal capture of intravenously injected TNP–Ficoll, and binding was unaffected by CD97 deficiency (Extended Data Fig. 7e,f). To test the impact of B cell CD97 deficiency on the antibody response, IgH^a:IgH^b mixed BM chimeras were generated by combining *Cd97*-KO (or control) IgH^b BM with BM from WT mice congenic for the IgH^a locus. Flow cytometric analysis confirmed that, compared to their frequency in control mixed chimeras, *Cd97*-KO IgH^b MZ B cells were reduced in WT IgH^a:*Cd97*-KO IgH^b mixed chimeras (Extended Data Fig. 7g). At day 6 after TNP–Ficoll immunization, serum was collected, and the amount of TNP binding IgM^a and IgM^b was measured. Although the production of TNP-specific IgM^a from WT cells was equivalent in each type of mixed BM chimera, the production of TNP-specific IgM^b by *Cd97*-KO cells was significantly reduced (Fig. 7d). Immunization of the same types of mixed chimeras with the T cell-dependent antigen NP-CGG led to IgM and IgG1 responses at day 12 that were unaffected by CD97 deficiency (Fig. 7e,f). Finally, we examined the IgM response to TNP–Ficoll in CD97-deficient mice and found that it was reduced (Fig. 7g). Thus, CD97 is required for mounting an intact early IgM response against a blood-borne polysaccharide antigen.

Discussion

MZ B cells migrate extensively within the blood-exposed MZ, yet they are rarely lost into blood circulation. Here, we show that MZ B cells sense their exposure to blood flow through interactions with passing RBCs using the CD55–CD97 ligand–receptor system. In the absence of CD97, CD55 or downstream signaling proteins $G\alpha_{13}$ and ARHGEF1, MZ B cell homeostasis in the spleen cannot be maintained due to cell loss into blood circulation. MZ B cell CD97 engagement by passing $CD55^+$ RBCs leads to extraction of the inhibitory CD97 NTF and activation of the receptor. In vitro studies in transfected cells establish that CD97 signaling causes Rho activation and cell membrane retraction, and we speculate that this retraction response favors MZ B cell retention in the MZ rather than movement into blood flow. This guidance system is important in allowing the spleen to mount serum IgM responses to blood-borne T cell-independent antigens.

The adhesion GPCR family has 33 members[13,40]. Recent structural studies of six family members have provided support for the conclusion that activation of the GPCR domain occurs after binding of a tethered ligand that corresponds to the residues immediately following the GPS[41]. The structures indicate that exposure of the tethered ligand can occur by removal of the NTF or possibly by it undergoing a conformational change that frees the tethered ligand for access to the GPCR binding site. Our studies suggest that CD97 activation involves NTF extraction. However, because the exposure to RBCs in vitro or in vivo only causes a partial reduction in CD97 staining, we do not exclude the possibility that receptor activation may also occur by conformational change without NTF extraction.

An important question is whether the interaction strength between CD55 and CD97 is strong enough for NTF extraction to occur. A recent structural study found that the total buried surface for the human CD97–CD55 interaction was 1,920 Å (ref. 2), an interface area above the average for protein–protein interactions[42]. Moreover, the authors noted that the architecture of the CD55–CD97 binding interface leads to a shearing stretch geometry that is predicted to resist force applied to the protein interface. Affinity measurements have not been made under shear stress conditions, and thus information is not yet available for the relevant off rate of the interaction. It is possible that catch bonds (that is, bonds whose k_{off} decreases with increasing force) strengthen the interaction under shear stress conditions. Selectin–ligand binding strength is increased under appropriate shear stress conditions due to catch bonds[43]. Moreover, EGF domains can participate in catch bond formation[44].

The retention of MZ B cells in the MZ depends on $\alpha_L\beta_2$ and $\alpha_4\beta_1$ integrins and the ligands ICAM1 and VCAM1 (ref. 9). Integrins are mechanosensitive receptors[45], and their activity in MZ B cells may be promoted by the fluid shear stress experienced by the cells. We suggest that when MZ B cells move into regions of the MZ (or adjacent red pulp) with higher amounts of fluid flow, the encounter with RBCs and subsequent signaling via CD97 to Rho may cause an increase in integrin-mediated adhesion[46,47]. Increased adhesion may cooperate with Rho-mediated leading-edge retraction to favor cell retention and movement away from the region of high blood flow. The CD97 PBM contributed to membrane retraction in transfected HEK293T cells, in agreement with earlier data showing that it binds cytoskeletal proteins[21]. Although our tether force and RhoA activation measurements in HEK293T cells were consistent with the C-terminal motif having a functional role, it should be noted that these studies were performed with mScarlet fused to the CD97 C terminus, and this may have obstructed PDZ domain access. Further studies will be needed to define the role of this motif in MZ B cells.

CD97 pathway deficiency led to a reduction in the serum IgM response to a blood-borne T cell-independent antigen most likely due to the combined effects of reduced numbers of MZ B cells and the reduced ability of the remaining MZ B cells to encounter the antigen. We suggest that the reduced TNP–Ficoll encounter by the remaining cells is because they are more deeply lodged among other MZ cells and are less exposed to blood flow. Our data indicate that $G\alpha_{13}$ and ARHGEF1 function downstream of CD97 to support behaviors needed for efficient blood-borne antigen capture. However, we note that these signaling molecules have roles downstream of additional receptors, and this likely explains the broader B cell response defects that have been observed in some studies of $G\alpha_{13}$- and ARHGEF1-deficient mice[27,48,49].

The human spleen has a more complex MZ architecture than the mouse spleen, and the cellular dynamics are less understood[1,3,32]. However, a marginal sinus has been identified, and at least some regions of the MZ are exposed to the open blood circulation[50]. Moreover, splenectomy in humans is associated with a reduced ability to control systemic infections by encapsulated bacteria[3], and human MZ B cells are involved in responses against bacterially derived polysaccharides[32]. Our finding of high CD97 expression on human MZ B cells and sensitivity of the NTF to extraction by engagement with RBCs raise the possibility that the pathway we identified in mice may also be involved in human spleen function in responding to blood-borne pathogens. Future studies, for example, with CD97-blocking reagents in primates, will be needed to understand the importance of this pathway in humans.

Online content

Any methods, additional references, Nature Portfolio reporting summaries, source data, extended data, supplementary information, acknowledgements, peer review information; details of author contributions and competing interests; and statements of data and code availability are available at https://doi.org/10.1038/s41590-023-01690-z.

References

1. Mebius, R. E. & Kraal, G. Structure and function of the spleen. *Nat. Rev. Immunol.* **5**, 606–616 (2005).
2. Arnon, T. I. & Cyster, J. G. Blood, sphingosine-1-phosphate and lymphocyte migration dynamics in the spleen. *Curr. Top. Microbiol. Immunol.* **378**, 107–128 (2014).
3. Lewis, S. M., Williams, A. & Eisenbarth, S. C. Structure and function of the immune system in the spleen. *Sci. Immunol.* **4**, eaau6085 (2019).
4. Martin, F. & Kearney, J. F. Marginal-zone B cells. *Nat. Rev. Immunol.* **2**, 323–335 (2002).
5. Allman, D. & Pillai, S. Peripheral B cell subsets. *Curr. Opin. Immunol.* **20**, 149–157 (2008).
6. Cinamon, G. et al. Sphingosine 1-phosphate receptor 1 promotes B cell localization in the splenic marginal zone. *Nat. Immunol.* **5**, 713–720 (2004).
7. Cinamon, G., Zachariah, M., Lam, O. & Cyster, J. G. Follicular shuttling of marginal zone B cells facilitates antigen transport. *Nat. Immunol.* **9**, 54–62 (2008).
8. Arnon, T. I., Horton, R. M., Grigorova, I. L. & Cyster, J. G. Visualization of splenic marginal zone B-cell shuttling and follicular B-cell egress. *Nature* **493**, 684–688 (2013).
9. Lu, T. T. & Cyster, J. G. Integrin-mediated long-term B cell retention in the splenic marginal zone. *Science* **297**, 409–412 (2002).
10. Cerutti, A., Cols, M. & Puga, I. Marginal zone B cells: virtues of innate-like antibody-producing lymphocytes. *Nat. Rev. Immunol.* **13**, 118–132 (2013).
11. Hammad, H. et al. Transitional B cells commit to marginal zone B cell fate by Taok3-mediated surface expression of ADAM10. *Nat. Immunol.* **18**, 313–320 (2017).
12. Langenhan, T., Aust, G. & Hamann, J. Sticky signaling—adhesion class G protein-coupled receptors take the stage. *Sci. Signal.* **6**, re3 (2013).
13. Purcell, R. H. & Hall, R. A. Adhesion G protein-coupled receptors as drug targets. *Annu. Rev. Pharmacol. Toxicol.* **58**, 429–449 (2018).
14. Vizurraga, A., Adhikari, R., Yeung, J., Yu, M. & Tall, G. G. Mechanisms of adhesion G protein-coupled receptor activation. *J. Biol. Chem.* **295**, 14065–14083 (2020).
15. Hamann, J., Vogel, B., van Schijndel, G. M. & van Lier, R. A. The seven-span transmembrane receptor CD97 has a cellular ligand (CD55, DAF). *J. Exp. Med.* **184**, 1185–1189 (1996).
16. Karpus, O. N. et al. Shear stress-dependent downregulation of the adhesion-G protein-coupled receptor CD97 on circulating leukocytes upon contact with its ligand CD55. *J. Immunol.* **190**, 3740–3748 (2013).
17. Liu, D. et al. CD97 promotes spleen dendritic cell positioning and homeostasis through sensing of red blood cells. *Science* **375**, eabi5965 (2022).
18. Wang, T. et al. Improved antibacterial host defense and altered peripheral granulocyte homeostasis in mice lacking the adhesion class G protein receptor CD97. *Infect. Immun.* **75**, 1144–1153 (2007).
19. Veninga, H. et al. Analysis of CD97 expression and manipulation: antibody treatment but not gene targeting curtails granulocyte migration. *J. Immunol.* **181**, 6574–6583 (2008).
20. Veninga, H. et al. A novel role for CD55 in granulocyte homeostasis and anti-bacterial host defense. *PLoS ONE* **6**, e24431 (2011).
21. Hilbig, D. et al. Mechano-dependent phosphorylation of the PDZ-binding motif of CD97/ADGRE5 modulates cellular detachment. *Cell Rep.* **24**, 1986–1995 (2018).
22. Dates, A. N. et al. A fusion protein platform for analyzing tethered agonism in the adhesion family of G protein-coupled receptors. Preprint at *bioRxiv* https://doi.org/10.1101/2022.07.14.500097 (2022).
23. Ward, Y. et al. LPA receptor heterodimerizes with CD97 to amplify LPA-initiated Rho-dependent signaling and invasion in prostate cancer cells. *Cancer Res.* **71**, 7301–7311 (2011).
24. Bhudia, N. et al. G protein-coupling of adhesion GPCRs ADGRE2/EMR2 and ADGRE5/CD97, and activation of G protein signalling by an anti-EMR2 antibody. *Sci. Rep.* **10**, 1004 (2020).
25. Rieken, S. et al. G_{12}/G_{13} family G proteins regulate marginal zone B cell maturation, migration, and polarization. *J. Immunol.* **177**, 2985–2993 (2006).
26. Aittaleb, M., Boguth, C. A. & Tesmer, J. J. Structure and function of heterotrimeric G protein-regulated Rho guanine nucleotide exchange factors. *Mol. Pharmacol.* **77**, 111–125 (2010).
27. Girkontaite, I. et al. Lsc is required for marginal zone B cells, regulation of lymphocyte motility and immune responses. *Nat. Immunol.* **2**, 855–862 (2001).
28. Dho, S. H., Lim, J. C. & Kim, L. K. Beyond the role of CD55 as a complement component. *Immune Netw.* **18**, e11 (2018).
29. Russell, E. S. & Bernstein, S. E. in *Biology of the Laboratory Mouse* Vol. 2 (ed. Green, E. L.) Ch. 17 (Dover Publications, 1966).
30. Das, N., Biswas, B. & Khera, R. Membrane-bound complement regulatory proteins as biomarkers and potential therapeutic targets for SLE. *Adv. Exp. Med. Biol.* **735**, 55–81 (2013).
31. Ley, K., Lundgren, E., Berger, E. & Arfors, K. E. Shear-dependent inhibition of granulocyte adhesion to cultured endothelium by dextran sulfate. *Blood* **73**, 1324–1330 (1989).
32. Weill, J. C., Weller, S. & Reynaud, C. A. Human marginal zone B cells. *Annu. Rev. Immunol.* **27**, 267–285 (2009).
33. Siu, J. H. Y. et al. Two subsets of human marginal zone B cells resolved by global analysis of lymphoid tissues and blood. *Sci. Immunol.* **7**, eabm9060 (2022).
34. Maddox, A. S. & Burridge, K. RhoA is required for cortical retraction and rigidity during mitotic cell rounding. *J. Cell Biol.* **160**, 255–265 (2003).
35. Dai, J. & Sheetz, M. P. Mechanical properties of neuronal growth cone membranes studied by tether formation with laser optical tweezers. *Biophys. J.* **68**, 988–996 (1995).
36. Heinrich, V. & Waugh, R. E. A piconewton force transducer and its application to measurement of the bending stiffness of phospholipid membranes. *Ann. Biomed. Eng.* **24**, 595–605 (1996).
37. Piekny, A. J. & Glotzer, M. Anillin is a scaffold protein that links RhoA, actin, and myosin during cytokinesis. *Curr. Biol.* **18**, 30–36 (2008).
38. van den Eertwegh, A. J., Laman, J. D., Schellekens, M. M., Boersma, W. J. & Claassen, E. Complement-mediated follicular localization of T-independent type-2 antigens: the role of marginal zone macrophages revisited. *Eur. J. Immunol.* **22**, 719–726 (1992).
39. Jahr, H., Hering, B., Federlin, K. & Bretzel, R. G. Activation of human complement by collagenase and ficoll. *Exp. Clin. Endocrinol. Diabetes* **103**, 27–29 (1995).
40. Hamann, J., Hsiao, C. C., Lee, C. S., Ravichandran, K. S. & Lin, H. H. Adhesion GPCRs as modulators of immune cell function. *Handb. Exp. Pharmacol.* **234**, 329–350 (2016).
41. Boucard, A. A. Self-activated adhesion receptor proteins visualized. *Nature* **604**, 628–630 (2022).
42. Niu, M. et al. Structural basis for CD97 recognition of the decay-accelerating factor CD55 suggests mechanosensitive activation of adhesion GPCRs. *J. Biol. Chem.* **296**, 100776 (2021).
43. McEver, R. P. & Zhu, C. Rolling cell adhesion. *Annu. Rev. Cell Dev. Biol.* **26**, 363–396 (2010).
44. Luca, V. C. et al. Notch–Jagged complex structure implicates a catch bond in tuning ligand sensitivity. *Science* **355**, 1320–1324 (2017).
45. Kanchanawong, P. & Calderwood, D. A. Organization, dynamics and mechanoregulation of integrin-mediated cell–ECM adhesions. *Nat. Rev. Mol. Cell Biol.* **24**, 142–161 (2023).

46. Laudanna, C., Campbell, J. J. & Butcher, E. C. Role of Rho in chemoattractant-activated leukocyte adhesion through integrins. *Science* **271**, 981–983 (1996).
47. Yeung, J. et al. GPR56/ADGRG1 is a platelet collagen-responsive GPCR and hemostatic sensor of shear force. *Proc. Natl Acad. Sci. USA* **117**, 28275–28286 (2020).
48. Rubtsov, A. et al. Lsc regulates marginal-zone B cell migration and adhesion and is required for the IgM T-dependent antibody response. *Immunity* **23**, 527–538 (2005).
49. Muppidi, J. R. et al. Loss of signalling via $G\alpha_{13}$ in germinal centre B-cell-derived lymphoma. *Nature* **516**, 254–258 (2014).
50. Kashimura, M. The human spleen as the center of the blood defense system. *Int. J. Hematol.* **112**, 147–158 (2020).

Methods

Mice

B6 (NCI 556) and B6-Ly5.1 (CD45.1; NCI 564) mice were purchased from the National Institute at Charles River at age 6–8 weeks. *Mpl*$^{-/-}$ (MGI, 3763248) mice were provided by M. R. Looney (University of California, San Francisco; UCSF). *Rag1*$^{-/-}$ (JAX, 002216; B6.129S7-*Rag1*^{tm1Mom}/J) mice were provided by A. Ma (UCSF). *Mb1-cre* mice (JAX, 020505; B6.C(Cg)-*Cd79a*$^{tm1(cre)Reth}$/EhobJ), IgH^a congenic B6 mice (JAX, 001317; B6.Cg-*Gpi1*^{a} *Thy1*^{a} *Igh*^{a}/J), *Adgre5*$^{-/-}$ mice[17], *Cd55*$^{-/-}$ mice[17], *Arhgef1*$^{-/-}$ mice[51], *Gna13*$^{fl/fl}$ mice[52], Ub-GFP mice (JAX, 004353; Tg(UBC-GFP)30Scha/J) and *Cd19*$^{-/-}$ mice[53] were from the internal colony. All mice were on a C57BL/6 background. All mice were housed in a specific pathogen-free environment at the Laboratory of Animal Research Center at UCSF, and all animal procedures were approved by the UCSF Institutional Animal Use and Care Committee. Mice of both sexes were used within an age range of 8–22 weeks. To block CD97, mice were treated with 30 µg of purified anti-CD97 (MAB33734, R&D) injected intravenously, and mice were analyzed 3 h or 4 d after treatment. For BM chimeras, mice were irradiated with 5.5 Gy of γ-irradiation in two doses 3 h apart and then intravenously transferred with BM cells from donors of the indicated genotypes. Chimeras were analyzed 8–12 weeks after reconstitution. In vivo pulse labeling was performed by injecting 1 µg of PE-conjugated anti-CD45.1 or anti-CD45.2 intravenously, and mice were analyzed after 3 min. Mice were allocated to control and experimental groups randomly. No statistical methods were used to predetermine sample sizes, but our sample sizes are similar to those reported in previous publications[8,48,54]. Data collection and analysis were not performed blind to the conditions of the experiments. No data points were excluded from the analyses for any reason. No animals were excluded except in rare cases where BM chimeras became sick before they could be used in an experiment.

Retroviral constructs and BM transductions

The CD97 gene *Adgre5* encodes isoforms of CD97 with different numbers of N-terminal EGF domains, with ADGRE5 (1,2,x,3,4, where x is a short peptide) and ADGRE5 (1,2,4) being the prominent isoforms. CD55 interacts predominantly with CD97 EGF domains 1 and 2, and it binds to all of the isoforms[42,55]. By performing PCR on cDNA prepared from sorted WT MZ B cells, we found that ADGRE5 (1,2,4) was abundant (unpublished observations), and we therefore used this variant for our studies. The use of the shorter variant allowed for improved expression from retroviral constructs. ADGRE5 (1,2,4) and its mutants joined to Thy1.1 by a 2A self-cleaving peptide sequence or ADGRE5 (1,2,4) with a C-terminal GFP fusion were inserted into a pQEF Moloney murine leukemia virus retroviral vector that incorporates an *EF1* promoter for improved expression. The Plat-E cell line, a gift from S. R. Schwab (New York University), was used to package virus. To prepare for the BM transduction, donor mice were intravenously injected with 3 mg of 5-fluorouracil (Sigma). BM was collected after 4–5 d and cultured with complete DMEM supplemented with interleukin-3 (IL-3), IL-6 and stem cell factor. BM cells were spin infected at days 1 and 2 and were subsequently injected into irradiated recipients after the second infection.

Immunizations

For the TNP–Ficoll uptake assay, 40 µg of TNP–Ficoll (Biosearch Technologies) was intravenously injected into each mouse 40 min before analysis. For analysis of the early antibody response, chimeras were immunized with 10 µg of TNP–Ficoll intravenously, and serum was collected 5–6 d after immunization. For analysis of T cell-dependent antibody responses, chimeras were treated with 50 µg of NP-CGG (Biosearch Technologies) in 50 µl of aluminum hydroxide gel by intraperitoneal injection, and serum was collected 12 d after immunization. TNP- or NP-specific antibodies were measured by ELISA using plates coated with TNP- or NP-BSA (Biosearch Technologies). TNP- or NP-specific antibodies were detected with biotinylated antibodies to mouse IgM^a (DS-1, 553515; 1:300), IgM^b (AF6-78, 553519; 1:300), IgG1^a (10.9, 553500; 1:300) and IgG1^b (B68-2, 553533, BD Biosciences; 1:300), followed by peroxidase-conjugated streptavidin (016-030-084, 1 mg ml^{-1}, Jackson ImmunoResearch; 1:500). ELISA plates were developed using a Substrate Reagent Pack (R&D) and read on a VERSA MAX microplate reader at an optical density of 450 nm.

Immunofluorescence staining

Spleen tissue cryosections (10 µm) were fixed in acetone for 10 min, dried for 1 h and subjected to staining with goat anti-IgD, AF647-conjugated anti-IgM (RMM-1, 406526; 1:100), APC-conjugated anti-IgM^a (MA-69, 408613; 1:100) and PE-conjugated anti-IgM^b (AF6-78, 406208; 1:100) from Biolegend and AMCA-conjugated donkey anti-goat IgG (H + L; 705-155-147, 0.5 mg ml^{-1}; 1:200) from Jackson Immunoresearch. Images were captured using a Zeiss AxioOberver Z1 inverted microscope and stitched together using ZEN 2 (blue edition).

Flow cytometry

Single-cell suspensions of splenic cells were prepared and stained with antibodies of indicated specificities in MACS buffer (PBS and 1% fetal bovine serum). The antibodies used for staining were BV785-conjugated anti-B220 (RA3-6B2, 103246; 1:200), BV605-conjugated anti-CD19 (6D5, 115540; 1:200), Pacific Blue-conjugated anti-CD21/CD35 (7E9, 123414; 1:200), PE/Cy7-conjugated anti-CD23 (B3B4, 101614; 1:200), PE-conjugated anti-CD5 (53-7.3, 100608; 1:200), PerCP-Cy5.5-conjugated anti-IgM (RMM-1, 406512; 1:200), PE-conjugated anti-CD45.2 (104, 109808; 1:200), FITC-conjugated anti-CD45.1 (A20, 110706; 1:200), FITC-conjugated anti-CD1d (1B1, 123508; 1:200), APC-conjugated anti-TER-119 (TER-119, 116212; 1:200), FITC-conjugated anti-CD41 (MWReg30, 133903; 1:200), PE-conjugated anti-IgD (IA6-2, 348204; 1:200), Pacific Blue-conjugated anti-IgM (MHM-88, 314514; 1:200), AF700-conjugated anti-CD1c (L161, 331529; 1:200) and FITC-conjugated anti-CD27 (M-T271, 356404; 1:200) from Biolegend; APC hamster IgG1 isotype control (anti-TNP, A19-3, 553974; 1:200), AF647-conjugated anti-Ki-67 (B56, 558615; 1:200) and PE hamster IgG1 isotype control (anti-TNP, A19-3, 553972; 1:200) from BD Biosciences; PE-conjugated anti-CD55 (REA300, 130-104-023; 1:100), APC-conjugated anti-CD97 (REA678, 130-110-229; 1:100), Annexin V-FITC (130-093-060; 1:200), APC-conjugated anti-CD97 (REA1242, 130-124-980; 1:100) and APC-conjugated anti-CD55 (REA1231, 130-124-497; 1:100) from Miltenyi Biotec. Dead cell exclusion was based on Fixable Viability Dye eFluor 780 staining (eBioscience), and non-singlet events were excluded with FSC-W/FSC-H characteristics. All data were collected on an LSRII and Symphony A1 cytometer (BD) with BD FACSDIVA V8.0.1 and 9.0.2 and analyzed with FlowJo V10 (TreeStar).

RBC enrichment and transfusion

Blood (400 µl) was collected retro-orbitally from *CD55*$^{-/-}$ or *CD55*$^{+/+}$ mice into Alserver's solution. The blood was mixed and centrifuged at 100*g* for 10 min at 24 °C without brake. Platelet-rich plasma and leukocyte-rich buffy coat were removed, and the remaining *CD55*$^{-/-}$ or *CD55*$^{+/+}$ RBCs were transferred intravenously into the appropriate mice once per week. Mice were analyzed 4 weeks after blood transfusion.

Human samples and processing

Adult human splenic tissue was obtained from research-consented deceased organ donors at the time of organ acquisition for clinical transplantation through an institutional review board (IRB)-approved research protocol with Donor Network West, the organ procurement organization for Northern California, in collaboration with the UCSF Viable Tissue Acquisition Lab (VITAL) Core. The study and all VITAL core studies are UCSF IRB designated as non-human subjects research (UCSF Human Research Protection Program IRB, study 20-31618, reference 299695), as tissues are from deidentified deceased individuals. Splenic tissue was collected immediately after clinical organ procurement,

stored and transported in University of Wisconsin preservation medium on ice and delivered at the same time as organs for transplantation for immediate processing. Donor spleens were cut into small pieces and homogenized and filtered through a 100-µm cell strainer. RBCs were lysed, and samples were prepared as single-cell suspensions. Human blood was collected into heparin-coated tubes, and RBCs were enriched by centrifugation at 100*g* for 10 min without brake.

Shear flow model in vitro

To mimic shear flow in vitro, 100 µl of purified RBCs was introduced into 1.5-ml tubes containing splenocytes from mice or humans and shaken (Eppendorf ThermoMixer F1.5) at 24 °C at 1,000 r.p.m. (shear ~14 dyne cm^{-2}) or not agitated. Forty-five minutes later, cells were collected, lysed and analyzed for CD97 expression by flow cytometry.

Cell morphology in CD97-expressing HEK293T cells

HEK293T cells (originally from ATCC) were transfected with CD97 (WT)–GFP, CD97 (T419G)–GFP or CTF–GFP fusion constructs. Cell membranes (CellBrite Steady 550 Membrane Staining kit, Biotium), nucleus (Hoechst 33342, Thermo Fisher) and surface CD97 (APC-conjugated anti-CD97, Miltenyibiotec) were stained in live cells and imaged 40 h after transfection. Imaging was conducted with a STELLARIS 8 confocal microscope (Leica) with a water immersion ×20 objective lens at a *z* step of 1 µm. Images were processed with Imaris software (Bitplane). Longest diameters of transfected individual cells were measured with ImageJ.

Lentiviral constructs and generation of CD97-expressing cell lines

ADGRE5 (1,2,4), its mutant T419G or PBM (that lacks the C-terminal SSESGM) with a C-terminal Scarlet fusion was inserted into the pLenti-SFFV Puro Lentiviral vector. Anillin–GFP RhoA biosensor was cloned from pEGFP-RhoA Biosensor (a gift from M. Glotzer, University of Chicago, Addgene plasmid 68026) and inserted into the lentiviral vector. Lentivirus were generated by mixing the plasmids HIV-gag pol (4 µg), vesicular stomatitis virus G protein (0.57 µg) and the respective lentiviral constructs (4 µg) and incubating this transfection mix in optimum medium (Thermo Fisher) with 4 µl of Xtremegene (Clontech) for 20 min at room temperature. Transfection solution was then applied to a 10-cm tissue culture-treated dish with seeded 4.4×10^6 HEK293T cells. Supernatants were collected at 24 and 48 h after transfection, filtered through a 0.45-µm filter and supplemented with 20 mM HEPES (pH 7.4) and 20 µM polybrene before being aliquoted and frozen at −80 °C. HEK293T cells were sequentially transduced with the lentivirus by diluting 1:2 with complete medium (DMEM, 10% fetal bovine serum and 1% penicillin/streptomycin), centrifuged for 2 h at 935*g* at 37 °C, expanded and sorted.

Optical C-trap plasma membrane tension measurements

Plasma membrane tension measurements were performed using a C-Trap optical trapping instrument (Lumicks BV). An IR laser beam (50 mW, 1,064 nm) was tightly focused through a series of mirrors, beam expanders and a high-numerical-aperture objective lens (×63/1.2-NA, water immersion, Nikon) to form a steerable optical trap. Cells were immobilized in an Ibidi µ-slide 0.4 Luer glass bottom (Ibidi) treated with 100 µl of 20 µg ml^{-1} fibronectin (Sigma). Mouse CD55 protein (R&D) was biotinylated with an EZ-Link Micro Sulfo-NHS-LC-Biotinylation kit (Thermo Fisher), according to the manufacturer's instructions. To measure plasma membrane tension, polystyrene beads (2.2 µm, Spherotech) coated with 20 µg of biotinylated mouse CD55 were added to the cell culture medium inside the slide. The beads were briefly placed in contact with the cell membrane (30 s), and tethers were extruded by moving the bead away from the cell perpendicularly at a speed of 2 µm s^{-1}. Force measurements were performed in the Lumicks Bluelake software suite by capturing the exiting trapping light with a high-numerical-aperture condenser lens (×63/1.45-NA, oil immersion, Zeiss) and measuring bead displacement in the trap with position-sensitive detectors through back focal plane interferometry. Florescence imaging was performed at 488 nm (RhoA anillin reporter) and 561 nm (CD97 WT or CD97 T419G expression) λ as membrane tethers were being pulled to ascertain RhoA activation at the site of bead contact and membrane tether. For RhoA recruitment/activation analysis, a region of interest was drawn around the site of bead attachment and pulling. The intensity of the anillin–GFP RhoA biosensor was measured over time in the 488-nm florescence channel. The region of interest size was maintained for all images analyzed. Images were analyzed using Fiji and rendered as videos with Adobe AfterEffect. All videos are played back at 5 frames per s, and time stamps are presented in minutes:seconds.

Intravital imaging of MZ B cells in spleen

MZ B cells were imaged in *Cd19*$^{-/-}$ mice reconstituted with GFP B cells. CTV-labeled naive B cells (4×10^7) were adoptively transferred intravenously 1 or 2 d before imaging. PKH26 dye-labeled RBCs (50 µl) were intravenously injected 3 h before imaging. Texas Red dextran (70 kD) was intravenously injected 30 min before imaging. The basic setup and procedure for intravital two-photon imaging of mouse spleens were essentially the same as previously described[8]. Imaging was conducted with STELLARIS 8 (Leica) using a two-photon microscope equipped with two Chameleon lasers at a *z* step of 3 µm. The imaging depth under the capsule of the spleen was between ~ 50 µm and ~200 µm. For video acquisition, a series of images was collected every 20–35 s. Excitation wavelengths were 820 nm and 1,030 nm. Off-line analyses were conducted with Imaris V9.3.1 (Bitplane). Cell count was analyzed with Imaris automatic spot tracking aided by manual verification, and cell migration and interaction were analyzed and verified with manual tracking in three-dimensional views. To distinguish PKH26$^+$ RBCs from macrophages that had engulfed damaged PKH26$^+$ RBCs, we took advantage of the observation that the macrophages also phagocytosed circulating Texas Red dextran and were thus fluorescent in both the red and far-red channels and applied a filter to remove bright far-red fluorescent cells from red fluorescent cells. Image sequences were rendered as videos with Adobe AfterEffect. All videos are played back at 20 frames per s unless indicated otherwise, and time stamps are represented in minutes:seconds.

Statistical analysis

Statistics and graphing were performed with Prism 9.4.1 (GraphPad). Two-tailed Student's *t*-tests were used to compare endpoint means of different groups. In grouped analyses, ordinary two-way ANOVAs were performed, and the indicated *P* values are from individual *t*-tests with Sidak's multiple testing correction. When multiple comparisons were being performed, ordinary one-way ANOVAs with Tukey's multiple-comparisons tests were used. Data distribution was assumed to be normal, but this was not formally tested. Single-cell sequencing data were analyzed with the Seurat R package.

Reporting summary

Further information on research design is available in the Nature Portfolio Reporting Summary linked to this article.

Data availability

All data are available in the main text or the supplementary materials.

References

51. Francis, S. A., Shen, X., Young, J. B., Kaul, P. & Lerner, D. J. Rho GEF Lsc is required for normal polarization, migration, and adhesion of formyl-peptide-stimulated neutrophils. *Blood* **107**, 1627–1635 (2006).

52. Ruppel, K. M. et al. Essential role for $G\alpha_{13}$ in endothelial cells during embryonic development. *Proc. Natl Acad. Sci. USA* **102**, 8281–8286 (2005).
53. Rickert, R. C., Rajewsky, K. & Roes, J. Impairment of T-cell-dependent B-cell responses and B-1 cell development in CD19-deficient mice. *Nature* **376**, 352–355 (1995).
54. Balazs, M., Martin, F., Zhou, T. & Kearney, J. Blood dendritic cells interact with splenic marginal zone B cells to initiate T-independent immune responses. *Immunity* **17**, 341–352 (2002).
55. Hamann, J. et al. Characterization of the CD55 (DAF)-binding site on the seven-span transmembrane receptor CD97. *Eur. J. Immunol.* **28**, 1701–1707 (1998).

Acknowledgements

We thank S. Coughlin (UCSF) for ArhGEF1- and Gna13-deficient mice. We thank L. Qiu, S. Cleary and C. Conrad for help with human blood samples. D.L. thanks the Westlake Microscopy Core facility for advice regarding imaging analysis. We thank M. Huse and O. Weiner for help with the RhoA studies. We thank R. Ponnusamy and A. Salehi of Donor Network West and J. Du of the UCSF VITAL Core for logistical assistance, and we deeply thank the organ and tissue donors and their families for their incredible generosity in helping to advance scientific research. D.L. was supported by a CRI Irvington Postdoctoral Fellowship. B.Y.W. was supported by a Schmidt Science Fellowship and is currently supported by a CRI Irvington Postdoctoral Fellowship. J.G.C. is an investigator of the Howard Hughes Medical Institute. This work was supported, in part, by NIH grants R01 AI40098 and R01 AI45073 (to J.G.C.).

Author contributions

D.L. and J.G.C. conceived the project, designed the experiments, interpreted the results and wrote the manuscript. B.Y.W. performed optical C-trap plasma membrane tension and RhoA activity measurements. M.Y.C. and H.T. helped with the NTF extraction experiment with human spleen samples as provided by J.M.G. Y.X. performed the molecular biology experiments. J.A. genotyped mice.

Competing interests

J.G.C. is an advisor for Be Biopharma and owns stock in ALX Oncology. The other authors declare no competing interests.

Additional information

Extended data is available for this paper at https://doi.org/10.1038/s41590-023-01690-z.

Supplementary information The online version contains supplementary material available at https://doi.org/10.1038/s41590-023-01690-z.

Correspondence and requests for materials should be addressed to Dan Liu or Jason G. Cyster.

Peer review information *Nature Immunology* thanks Ziv Shulman, Marcus Thelen and the other, anonymous, reviewer(s) for their contribution to the peer review of this work. Primary Handling Editor: L. A. Dempsey, in collaboration with the *Nature Immunology* team.

https://doi.org/10.1038/s41590-023-01690-z

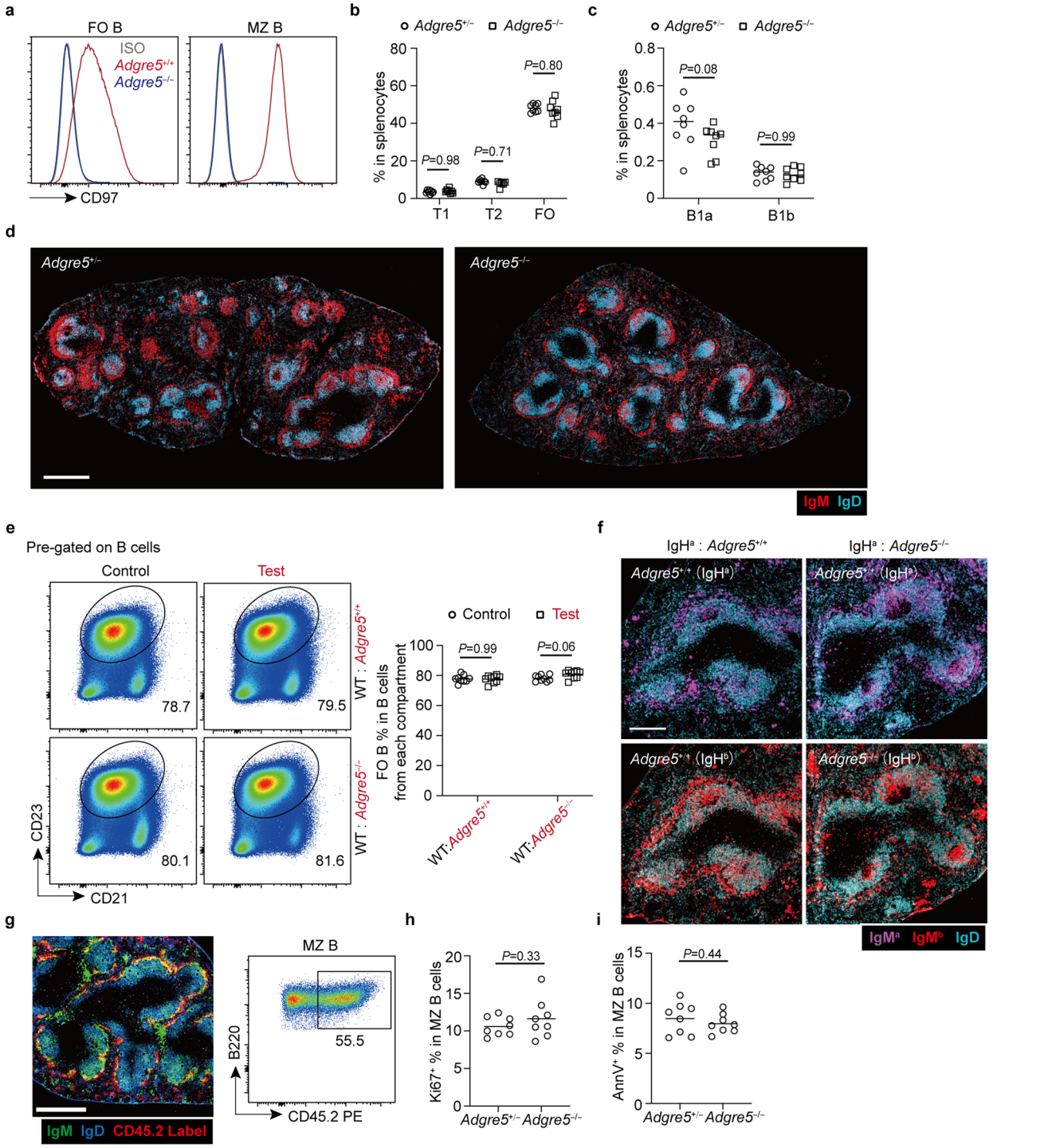

Extended Data Fig. 1 | CD97 requirements of splenic MZ B cells. a, Representative histogram plot of surface CD97 on FO B (left panel) and MZ B (right panel) cells in *Adgre5*$^{-/-}$ and control mice. **b**, Frequencies of T1, T2 and FO B cells in total splenocytes in *Adgre5*$^{-/-}$ (n = 8) and control (n = 8) mice. **c**, Frequencies of B1a and B1b cells in total splenocytes in *Adgre5*$^{-/-}$ (n = 8) and control (n = 8) mice. **d**, Representative distribution patterns of IgM^{hi} MZ B (red) relative to IgD^{hi} FO B cells (blue) in full spleen cross-sections from mice of the indicated genotypes. Multiple images are stitched to obtain the full spleen view. Scale bar, 500 µm. **e**, Mixed (50:50) bone marrow (BM) chimeras were made with CD45.1 WT (*Adgre5*$^{+/+}$) and CD45.2 *Adgre5*$^{+/+}$ or *Adgre5*$^{-/-}$ BM cells. Representative flow cytometry profiles (left panel) and frequencies (right panel) of FO B cells of indicated genotyped CD19^{+} B cells in WT:*Adgre5*$^{-/-}$ (n = 9) and its control (n = 9) mixed BM chimeras. **f**, Representative distribution patterns of IgM^{a} (magenta) and IgM^{b} MZ B (red) relative to FO B cells (blue) in spleens of 50:50 mixed IgH^{a} WT (*Adgre5*$^{+/+}$) with IgH^{b} *Adgre5*$^{+/+}$ or *Adgre5*$^{-/-}$ chimeras. Scale bar, 200 µm. **g**, Representative distribution patterns (left panel) and frequencies (right panel) of in vivo antibody labeling of MZ B cells (green) relative to FO B cells (blue) in spleens 3 min after i.v. injection of PE-conjugated anti-CD45.2 (red). Blood-exposed MZ B cells (cells that have bound CD45.2-PE) appear yellow. Scale bar, 200 µm. **h**,**i**, Frequencies of Ki-67^{+} (**h**) and Annexin^{+} (**i**) cells in MZ B cells in *Adgre5*$^{-/-}$ (n = 8) and control (n = 8) mice. Data are pooled from two independent experiments (**b**, **c**, **e**, **h**, **i**). Sections are representative of multiple cross-sections from at least three mice (**d**, **f**, **g**). Each symbol represents one mouse and lines denote means. Statistical significance was tested by two-way ANOVA followed by Sidak's multiple comparisons test (**b**, **c**, **e**) or two-tailed *t*-test (**h**, **i**).

https://doi.org/10.1038/s41590-023-01690-z

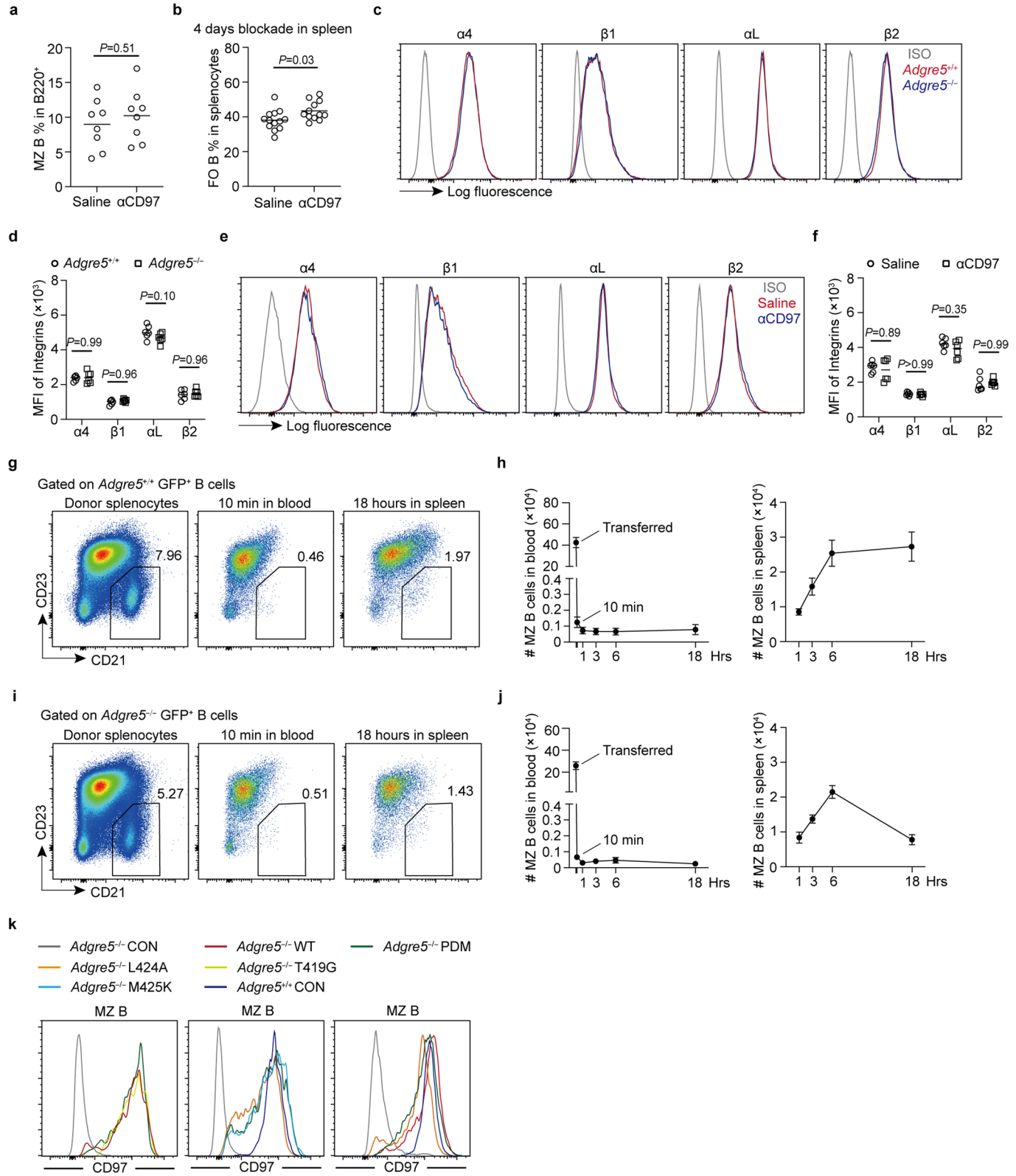

Extended Data Fig. 2 | See next page for caption.

https://doi.org/10.1038/s41590-023-01690-z

Extended Data Fig. 2 | CD97-deficient MZ B cells have disadvantage to re-seed the spleen. a, Frequencies of MZ B cells in splenic B220$^+$ B cells in WT mice 3 hours treatment with anti-CD97 antibody (n = 8) or saline (n = 8). **b**, Frequencies of FO B cells in spleen of WT mice 4 days after treatment with anti-CD97 antibody (n = 12) or saline (n = 13). **c**,**d**, Representative histogram plots (**c**) and MFI (**d**) of cell surface integrins on MZ B cells in *Adgre5*$^{-/-}$ (n = 6) and control (n = 6) mice. **e**,**f**, Representative histogram plots (**e**) and MFI (**f**) of cell surface integrins in WT mice after 4 days treatment with anti-CD97 antibody (n = 6) or saline (n = 6). **g**-**j**, *Adgre5*$^{+/+}$ GFP$^+$ (**g**, **h**) and *Adgre5*$^{-/-}$ GFP$^+$ (**i**,**j**) splenocytes were transferred into WT recipients and the number of donor MZ B cells in blood and spleen determined over time. (**g**,**h**) Representative flow cytometry profiles of MZ B cells among GFP$^+$ B cells (**g**) and cell counts (Mean ± SEM) of GFP$^+$ MZ B cells staying in blood (**h** left panel) and homing into the spleen (**h** right panel) were analyzed at indicated time points (n = 7 on 0 h, n = 8 on 0.17 h, n = 8 on 1 h, n = 8 on 3 h, n = 8 on 6 h, n = 7 on 18 h). (**i**,**j**) Representative flow cytometry profiles of MZ B cells among GFP$^+$ B cells (**i**) and cell counts (Mean ± SEM) of GFP$^+$ MZ B cells staying in blood (**j** left panel) and homing into the spleen (**j** right panel) were analyzed at indicated time points (n = 6 on 0 h, n = 8 on 0.17 h, n = 8 on 1 h, n = 8 on 3 h, n = 7 on 6 h, n = 8 on 18 h). The blood volume in all recipients was estimated as 2 ml. **k**, Representative histogram plots of surface CD97 on Thy1.1$^+$ CD45.2$^+$ MZ B cells in chimeras reconstituted as indicated. See corresponding Fig. 2k. Data are pooled from two (**a**, **d**, **f**, **h**, **j**) or three (**b**) independent experiments. Each symbol represents one mouse and lines denote means. Statistical significance was tested by two-tailed *t*-test (**a**, **b**) or two-way ANOVA followed by Sidak's multiple comparisons test (**d**, **f**).

https://doi.org/10.1038/s41590-023-01690-z

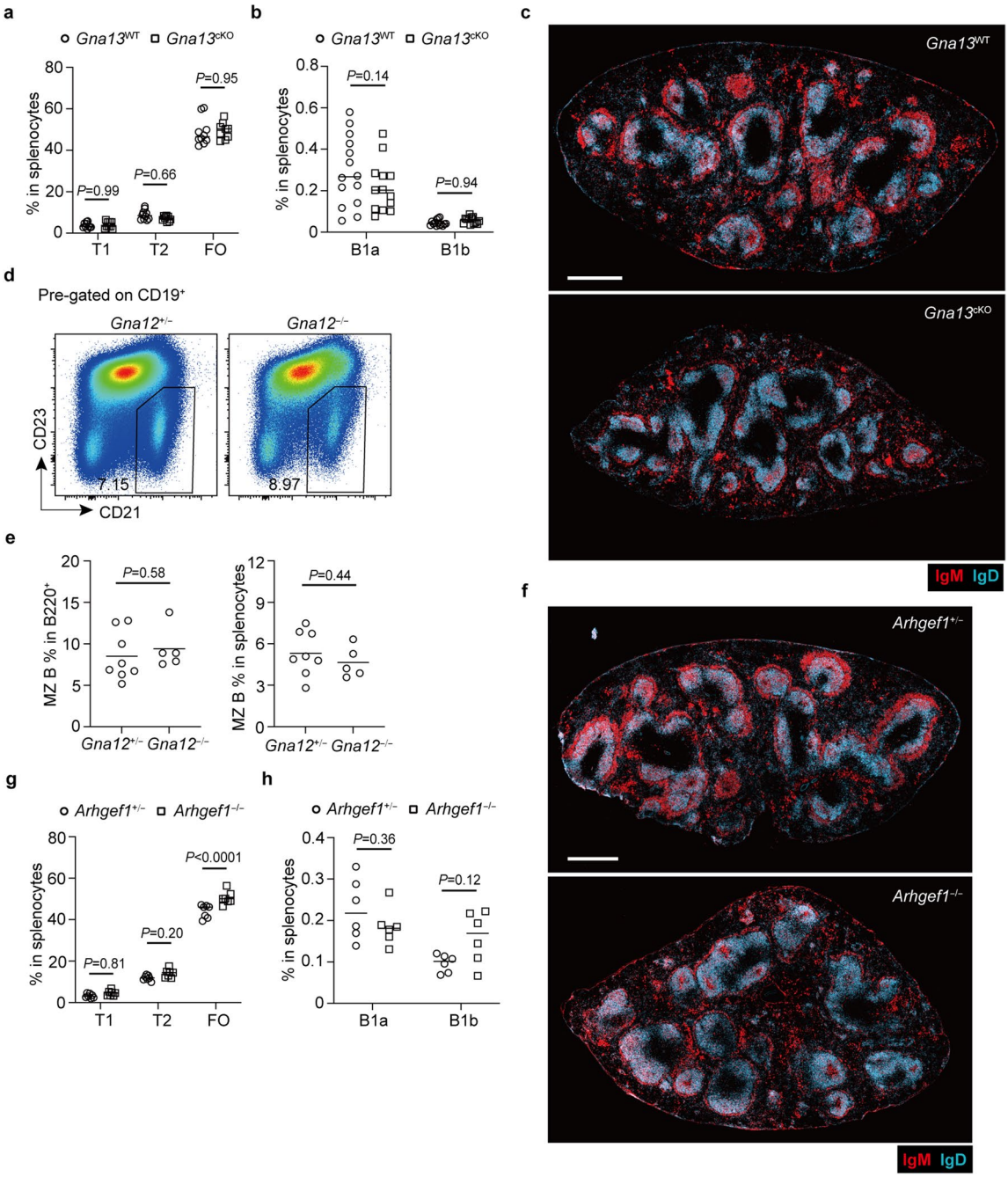

Extended Data Fig. 3 | Selective Gα13-ArhGEF1 requirements of splenic B cells. a, Frequencies of T1, T2 and FO B cells in total splenocytes in *Gna13*^{cKO} (n = 9) and control (n = 10) mice. **b**, Frequencies of B1a and B1b cells in total splenocytes in *Gna13*^{cKO} (n = 13) and control (n = 14) mice. **c**, Representative distribution patterns of IgM^{hi} MZ B (red) relative to IgD^{hi} FO B cells (blue) in full spleen cross-sections from mice of the indicated genotypes. Scale bar, 500 µm. **d**,**e**, Representative flow cytometry profiles (**d**) and frequencies of MZ B in total CD19^{+} B cells (**e** left panel), and in total splenocytes (**e** right panel) in *Gna12*$^{-/-}$ (n = 8) and control (n = 5) chimeras. **f**, Representative distribution patterns of IgM^{hi} MZ B (red) relative to IgD^{hi} FO B cells (blue) in full spleen cross-sections from mice of the indicated genotypes. Scale bar, 500 µm. **g**, Frequencies of T1, T2 and FO B cells in total splenocytes in *Arhgef1*$^{-/-}$ (n = 7) and control (n = 7) mice. **h**, Frequencies of B1a and B1b cells in total splenocytes in *Arhgef1*$^{-/-}$ (n = 6) and control (n = 6) mice. Data are pooled from two (**a**, **e**, **g**, **h**) or three (**b**) independent experiments. Sections are representative of multiple cross-sections from at least three mice of each type (**c**, **f**). Each symbol represents one mouse and lines denote means. Statistical significance was tested by two-way ANOVA followed by Sidak's multiple comparisons test (**a**, **b**, **g**, **h**) or two-tailed *t*-test (**e**).

https://doi.org/10.1038/s41590-023-01690-z

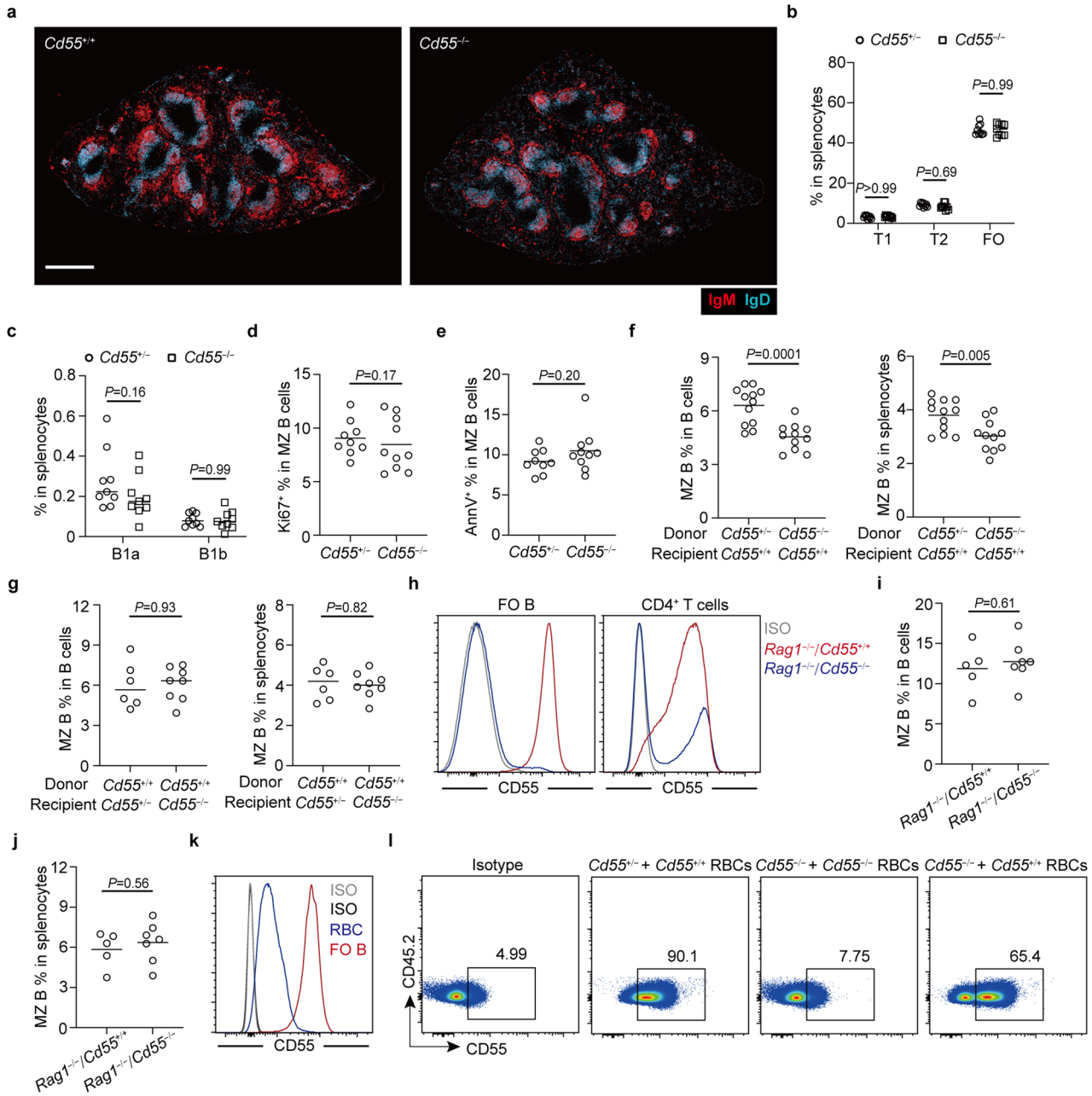

Extended Data Fig. 4 | CD55 requirements of splenic MZ B cells. a, Representative distribution patterns of IgM^{hi} MZ B (red) relative to IgD^{hi} FO B cells (blue) in full spleen cross-sections from mice of the indicated genotypes. Scale bar, 500 µm. Sections are representative of multiple cross-sections from at least three mice of each type. **b**, Frequencies of T1, T2 and FO B cells in total splenocytes in *Cd55*$^{-/-}$ (n = 9) and control (n = 9) mice. **c**, Frequencies of B1a and B1b cells in total splenocytes in *Cd55*$^{-/-}$ (n = 9) and control (n = 9) mice. **d**,**e**, Frequencies of Ki-67^{+} (**d**) and Annexin^{+} (**e**) cells in MZ B cells in *Cd55*$^{-/-}$ (n = 10) and control (n = 9) mice. **f**, Frequencies of MZ B cells in total CD19^{+} B cells (left panel), and in total splenocytes (right panel) in *Cd55*$^{-/-}$ (n = 11) and control (n = 12) chimeras as indicated. **g**, Frequencies of MZ B cells in total CD19^{+} B cells (left panel), and in total splenocytes (right panel) in *Cd55*$^{-/-}$ (n = 8) and control (n = 6) reverse chimeras as indicated. **h-j**, Chimeras reconstituted with 85% *Rag1*$^{-/-}$ and 15% *Cd55*$^{+/+}$ or *Cd55*$^{-/-}$ BM cells. (**h**) Representative histogram plot of surface CD55 on FO B cells (left panel) and CD4 T cells (right panel) in chimeras as indicated. (**i**,**j**) Frequencies of MZ B cells in total CD19^{+} B cells (**i**), and in total splenocytes (**j**) in *Rag1*$^{-/-}$: *Cd55*$^{-/-}$ (n = 7) and its control (n = 5) chimeras. **k**, Representative histogram plot of surface CD55 on FO B cells and RBCs. **l**, Representative profile of purified *Cd55*$^{+/+}$ RBCs or *Cd55*$^{-/-}$ RBCs transfused into the indicated recipient mice once per week for 4 weeks. Data are pooled from two (**b**-**e**, **g**, **i**, **j**) or three (**f**) independent experiments. Each symbol represents one mouse and lines denote means. Statistical significance was tested by two-way ANOVA followed by Sidak's multiple comparisons test (**b**, **c**) or two-tailed *t*-test (**d**-**g**, **i**, **j**).

https://doi.org/10.1038/s41590-023-01690-z

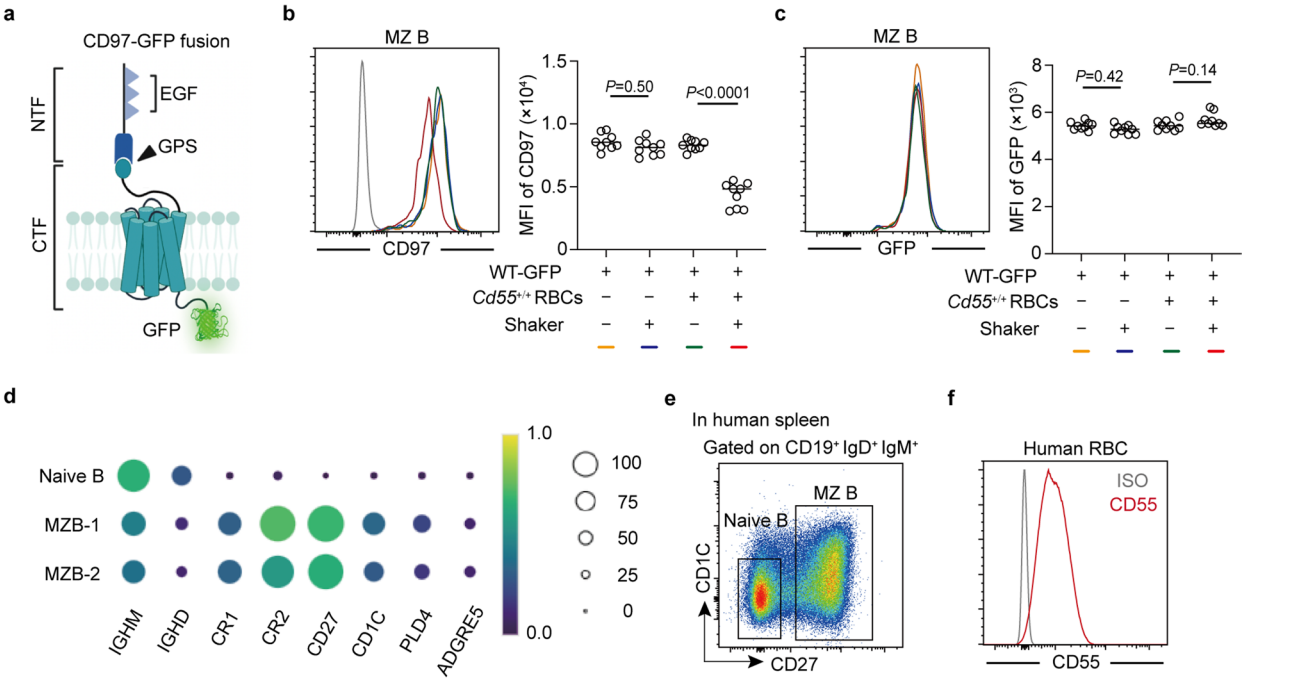

Extended Data Fig. 5 | CD55-mediated extraction of CD97 NTF under shear stress is conserved on human MZ B cells. a, Structural components of the CD97-GFP fusion protein. NTF, N-terminal fragment; CTF, C-terminal fragment; GPS, GPCR proteolysis site; triangles indicate individual epidermal growth factor (EGF) domains; GFP, Green fluorescent protein. **b**,**c**, Splenocytes from CD97-GFP fusion protein expressing BM chimeras were cocultured for 45 minutes at 24 °C with *Cd55*$^{+/+}$ RBCs, on a shaker or not. Representative histogram (left panel) and MFI (right panel) of surface CD97 expression (**b**) and GFP (**c**) on MZ B cells (n = 9 in each group). Data are pooled from two independent experiments. Each symbol represents one incubation and each donor contributes three incubations. Lines denote means, and line colors in histograms are for conditions of the types shown by color codes beneath the graphs. Statistical significance was tested by one-way ANOVA followed by Tukey's multiple comparisons test. **d**, Dot plot illustrating marker gene expression for human specific B cell subtypes. Data are from GSE193869 (ref. 33). **e**, Representative flow cytometry profiles displaying gates of human naïve and MZ B cells. **f**, Representative histogram plot of surface CD55 on human peripheral RBCs.

https://doi.org/10.1038/s41590-023-01690-z

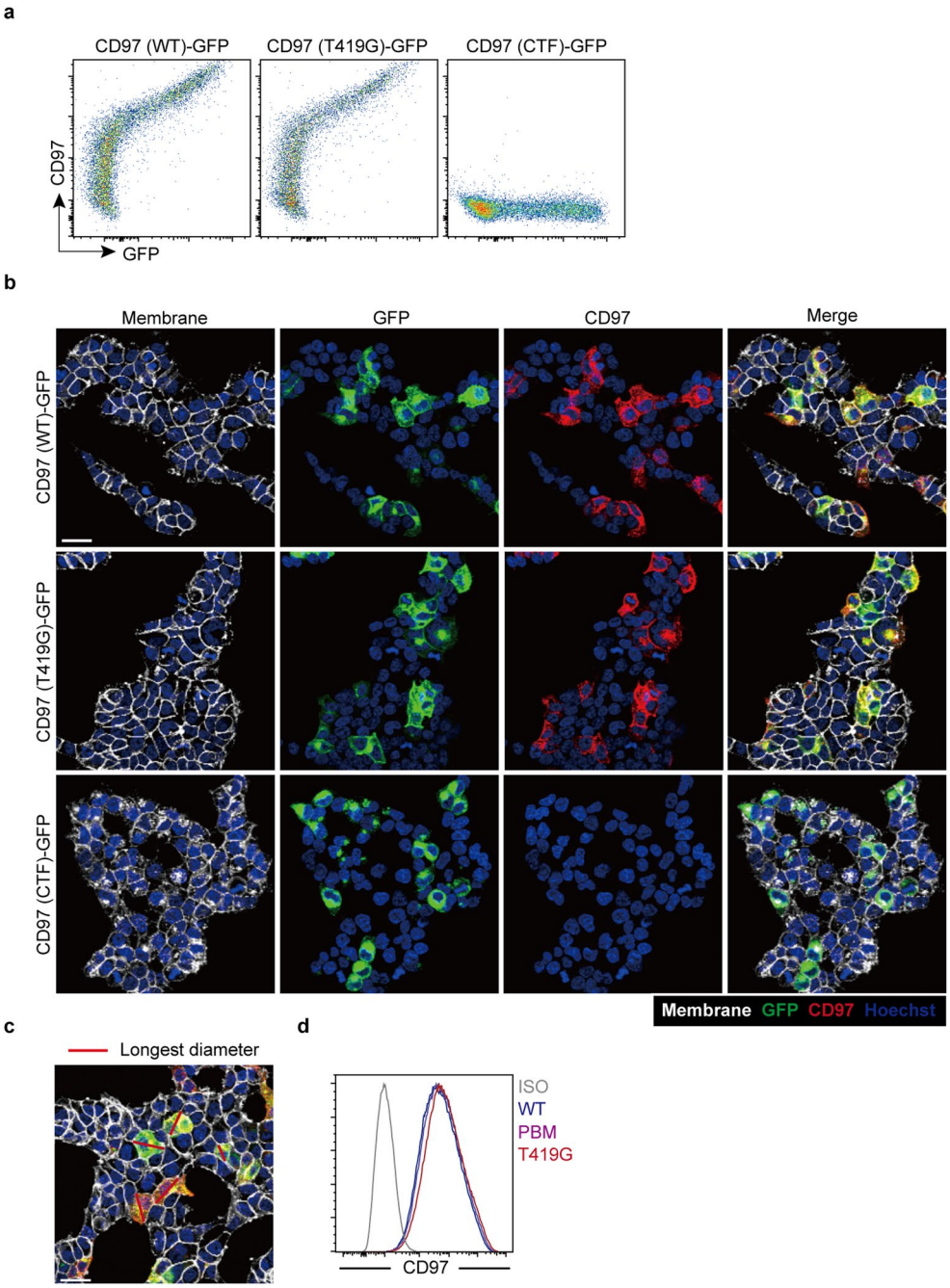

Extended Data Fig. 6 | CD97 promotes cell membrane retraction through activation of RhoA. a-c, HEK293T cells were transfected with CD97 (WT)-GFP, CD97 (T419G)-GFP, or CTF-GFP fusion constructs. (**a**) Representative flow cytometry profiles of CD97 and GFP in transfected HEK293T cells 40 hours post transfection. (**b**) Cell membranes, nucleus, GFP and surface CD97 were stained and imaged. Scale bar, 30 μm. Data are representative of three independent experiments. (**c**) Longest diameters of transfected individual cells were measured with ImageJ. **d**, HEK293T cells were co-transduced with Anillin-GFP RhoA Biosensor and CD97 (WT)-Scarlet, CD97 (T419G)-Scarlet, or CD97 (PBM)-Scarlet fusion lentivirus and sorted. Representative histogram plot of surface CD97 on sorted HEK293T cells.

https://doi.org/10.1038/s41590-023-01690-z

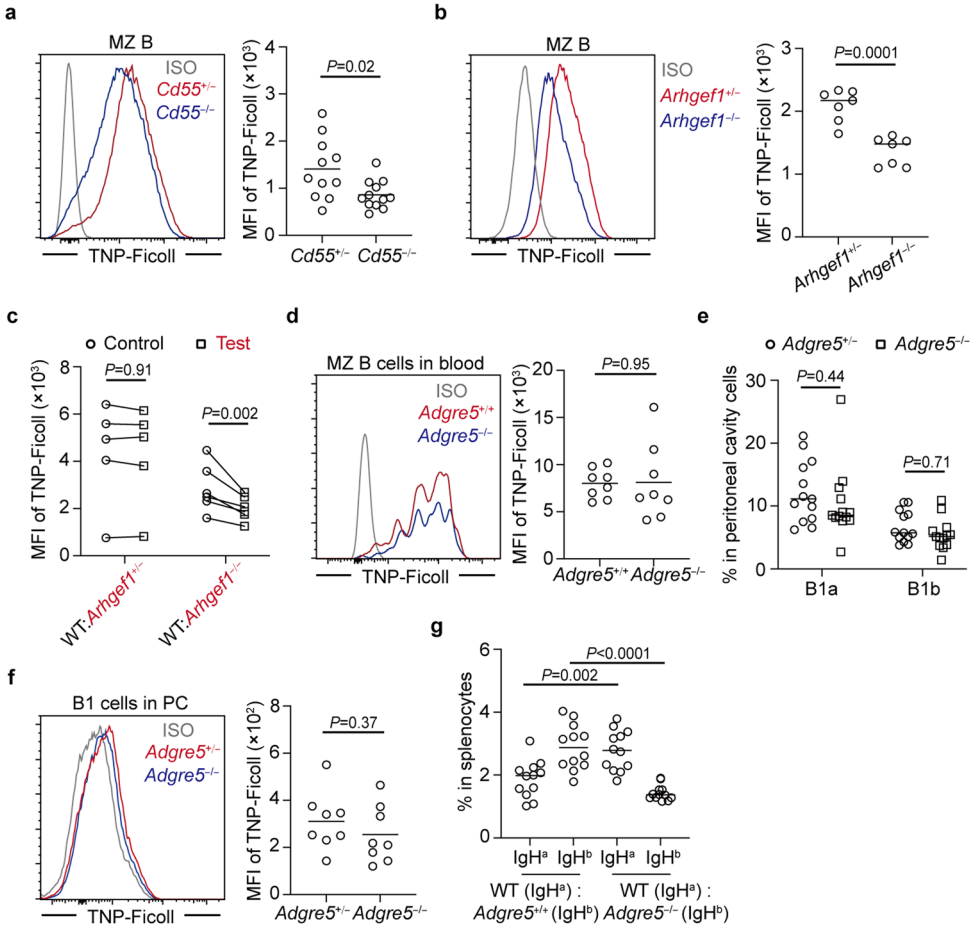

Extended Data Fig. 7 | CD97-pathway deficiency leads to defective early antibody responses to T-independent antigen. a-c, Mice were analyzed 40 minutes after intravenous TNP-Ficoll injection. (**a**) Representative histogram (left panel) and MFI (right panel) of TNP-Ficoll level on MZ B cells in *Cd55*$^{-/-}$ (n = 12) and control (n = 11) mice. (**b**) Representative histogram (left panel) and MFI (right panel) of TNP-Ficoll level on MZ B cells in *Arhgef1*$^{-/-}$ (n = 7) and control (n = 7) mice. (**c**) MFI of TNP-Ficoll level on MZ B cells in WT:*Arhgef1*$^{-/-}$ (n = 6) and its control (n = 5) mixed BM chimeras. Lines connect data from same animals. **d**, *Adgre5*$^{+/+}$ Ub-GFP^{+} or *Adgre5*$^{-/-}$ Ub-GFP^{+} splenocytes were transferred into WT mice. 10 minutes later, TNP-Ficoll was injected intravenously and GFP^{+} cells from blood were analyzed 40 minutes later for bound TNP-Ficoll. Representative histogram (left panel) and MFI (right panel) of TNP-Ficoll level on transferred *Adgre5*$^{-/-}$ (n = 8) and *Adgre5*$^{+/+}$ (n = 8) MZ B cells in blood. **e**, Frequencies of B1a and B1b cells in peritoneal cavity in *Adgre5*$^{-/-}$ (n = 13) and control (n = 13) mice. **f**, Representative histogram (left panel) and MFI (right panel) of TNP-Ficoll level on B1a and B1b cells in peritoneal cavity of *Adgre5*$^{-/-}$ (n = 8) and control (n = 8) mice 40 minutes after intravenous TNP-Ficoll immunization. (**g**) Frequencies of IgH^{a} WT (*Adgre5*$^{+/+}$), IgH^{b} *Adgre5*$^{+/+}$ (n = 12) or *Adgre5*$^{-/-}$ (n = 12) in total splenocytes of mixed chimeras. Data are pooled from three (**a**, **e**, **g**) or two (**b**-**d**, **f**) independent experiments. Each symbol represents one mouse and lines denote means. Statistical significance was tested by two-tailed *t*-test (**a**, **b**, **d**, **f**), or two-way ANOVA followed by Sidak's multiple comparisons test (**c**, **e**) or one-way ANOVA followed by Tukey's multiple comparisons test (**g**).

nature portfolio

Corresponding author(s): Jason G. Cyster; Dan Liu

Last updated by author(s): Oct 14, 2023

Reporting Summary

Nature Portfolio wishes to improve the reproducibility of the work that we publish. This form provides structure for consistency and transparency in reporting. For further information on Nature Portfolio policies, see our Editorial Policies and the Editorial Policy Checklist.

Statistics

For all statistical analyses, confirm that the following items are present in the figure legend, table legend, main text, or Methods section.

n/a	Confirmed	
☐	☒	The exact sample size (*n*) for each experimental group/condition, given as a discrete number and unit of measurement
☐	☒	A statement on whether measurements were taken from distinct samples or whether the same sample was measured repeatedly
☐	☒	The statistical test(s) used AND whether they are one- or two-sided *Only common tests should be described solely by name; describe more complex techniques in the Methods section.*
☐	☒	A description of all covariates tested
☐	☒	A description of any assumptions or corrections, such as tests of normality and adjustment for multiple comparisons
☐	☒	A full description of the statistical parameters including central tendency (e.g. means) or other basic estimates (e.g. regression coefficient) AND variation (e.g. standard deviation) or associated estimates of uncertainty (e.g. confidence intervals)
☐	☒	For null hypothesis testing, the test statistic (e.g. *F*, *t*, *r*) with confidence intervals, effect sizes, degrees of freedom and *P* value noted *Give P values as exact values whenever suitable.*
☒	☐	For Bayesian analysis, information on the choice of priors and Markov chain Monte Carlo settings
☒	☐	For hierarchical and complex designs, identification of the appropriate level for tests and full reporting of outcomes
☒	☐	Estimates of effect sizes (e.g. Cohen's *d*, Pearson's *r*), indicating how they were calculated

Our web collection on statistics for biologists contains articles on many of the points above.

Software and code

Policy information about availability of computer code

Data collection	Flow cytometry data were collected using BD FACSDIVA V8.0.1 and 9.0.2. IF data were collected using ZEN 2 (blue edition). Two photon imaging data were collected using STELLARIS 8.
Data analysis	Flowcytometry data were processed and analyzed using FlowJo V10. Imaging data were processed and analyzed using Imaris V9.3.1. Single cell sequencing data were analyzed using the Seurat R package. Statistics and graphing were done with Prism 9.4.1 (GraphPad).

For manuscripts utilizing custom algorithms or software that are central to the research but not yet described in published literature, software must be made available to editors and reviewers. We strongly encourage code deposition in a community repository (e.g. GitHub). See the Nature Portfolio guidelines for submitting code & software for further information.

Data

Policy information about availability of data

All manuscripts must include a data availability statement. This statement should provide the following information, where applicable:

- Accession codes, unique identifiers, or web links for publicly available datasets
- A description of any restrictions on data availability
- For clinical datasets or third party data, please ensure that the statement adheres to our policy

All data are available in the main text or the supplementary materials.

Research involving human participants, their data, or biological material

Policy information about studies with human participants or human data. See also policy information about sex, gender (identity/presentation), and sexual orientation and race, ethnicity and racism.

Reporting on sex and gender	We have two donors, one male and one female.
Reporting on race, ethnicity, or other socially relevant groupings	The male donor is Hispanic/Latino and the female donor is White.
Population characteristics	The male donor was 45 years old with gall bladder symptoms. The female donor was 53 years old. She saw s physician for Thyroid issues, and took vitamins and supplements.
Recruitment	Death from natural causes
Ethics oversight	Human splenic tissue was obtained from research-consented deceased organ donors at the time of organ acquisition for clinical transplantation through an IRB-approved research protocol with Donor Network West, the organ procurement organization for Northern California, in collaboration with the UCSF VIable Tissue Acquisition Lab (VITAL) Core. The study and all VITAL core studies are UCSF IRB-designated as non-human subjects research (UCSF Human Research Protection Program Institutional Review Board, study #20-31618, reference # 299695), as tissues are from de-identified deceased individuals.

Note that full information on the approval of the study protocol must also be provided in the manuscript.

Field-specific reporting

Please select the one below that is the best fit for your research. If you are not sure, read the appropriate sections before making your selection.

☒ Life sciences ☐ Behavioural & social sciences ☐ Ecological, evolutionary & environmental sciences

For a reference copy of the document with all sections, see nature.com/documents/nr-reporting-summary-flat.pdf

Life sciences study design

All studies must disclose on these points even when the disclosure is negative.

Sample size	Each sample size is indicated in the figure legend. Based on common experiences in the relevant disciplines, the sample size was set empirically to provide a reasonable statistical power of detecting biological effects. No statistical methods were used to pre-determine the sample size.
Data exclusions	No data were excluded from analyses.
Replication	All experimental findings were reproducible at least three independent experiments, as indicated in figure legends, unless explicitly indicated otherwise.
Randomization	Co-housed animals of indicated genotypes were randomly assigned to groups for comparison where applicable. Because of the relative immaturity of the marginal zone and its compartments, we chose adult humans with autoimmune diseases as donors.
Blinding	No blinding was involved in experiments, as there was no subjective measurement in these experiments.

Reporting for specific materials, systems and methods

We require information from authors about some types of materials, experimental systems and methods used in many studies. Here, indicate whether each material, system or method listed is relevant to your study. If you are not sure if a list item applies to your research, read the appropriate section before selecting a response.

Materials & experimental systems

n/a	Involved in the study
☐	☒ Antibodies
☐	☒ Eukaryotic cell lines
☒	☐ Palaeontology and archaeology
☐	☒ Animals and other organisms
☒	☐ Clinical data
☒	☐ Dual use research of concern
☒	☐ Plants

Methods

n/a	Involved in the study
☒	☐ ChIP-seq
☐	☒ Flow cytometry
☒	☐ MRI-based neuroimaging

Antibodies

Antibodies used

The antibodies used for staining were BV785-conjugated anti-B220 (RA3-6B2, Cat #103246, 1:200), BV605-conjugated anti-CD19 (6D5, Cat #115540, 1:200), Pacific Blue-conjugated anti-CD21/35 (7E9, Cat #123414, 1:200), PE/Cyanine7 conjugated anti-CD23 (B3B4, Cat #101614, 1:200), PE-conjugated anti-CD5 (53-7.3, Cat #100608, 1:200), PerCP-Cy5.5-conjugated anti-IgM (RMM-1, Cat #406512, 1:200), PE-conjugated anti-CD45.2 (104, Cat #109808, 1:200), FITC-conjugated anti-CD45.1 (A20, Cat #110706, 1:200), FITC-conjugated anti-CD1d (1B1, Cat #123508, 1:200), APC-conjugated anti-TER-119 (TER-119, Cat #116212, 1:200), FITC-conjugated anti-CD41 (MWReg30, Cat #133903, 1:200), PE-conjugated anti-IgD (IA6-2, Cat #348204, 1:200), Pacific Blue-conjugated anti-IgM (MHM-88, Cat #314514, 1:200), Alexa Fluor 700-conjugated anti-CD1c (L161, Cat #331529, 1:200), FITC-conjugated anti-CD27 (M-T271, Cat #356404, 1:200), Alexa Fluor 647-conjugated anti-IgM (RMM-1, Cat #406526, 1:100), APC-conjugated anti-IgMa (MA-69, Cat #408613, 1:100) and PE-conjugated anti-IgMb (AF6-78, Cat #406208, 1:100) from Biolegend; APC Hamster IgG1 isotype control (anti-TNP, A19-3, Cat #553974, 1:200), Alexa Fluor 647-conjugated anti-Ki-67 (B56, Cat #558615, 1:200), PE Hamster IgG1 isotype control (anti-TNP, A19-3, Cat #553972, 1:200), biotinylated anti-IgMa (DS-1, Cat #553515, 1:300), biotinylated anti-IgMb (AF6-78, Cat #553519, 1:300), biotinylated anti-IgG1a (10.9, Cat #553500, 1:300) and biotinylated anti-IgG1b (B68-2, Cat #553533, 1:300) from BD Biosciences; PE-conjugated anti-CD55 (REA300, Cat #130-104-023, 1:100), APC-conjugated anti-CD97 (REA678, Cat #130-110-229, 1:100), Annexin V-FITC (Cat #130-093-060, 1:200), APC-conjugated anti-CD97 (REA1242, Cat #130-124-980, 1:100) and APC-conjugated anti-CD55 (REA1231, Cat #130-124-497, 1:100) from Miltenyibiotec; AMCA-conjugated donkey anti-goat IgG (H+L) (Cat #705-155-147, 0.5 mg/ml, 1:200) and Peroxidase-conjugated Streptavidin (Cat #016-030-084,1 mg/ml, 1:500) from Jackson ImmunoResearch.

Validation

The specificity and application of these antibodies have been validated by the manufacturers on the website.
BV785-conjugated anti-B220
https://www.biolegend.com/fr-ch/products/brilliant-violet-785-anti-mouse-human-cd45r-b220-antibody-7960?GroupID=GROUP658
BV605-conjugated anti-CD19
https://www.biolegend.com/fr-fr/products/brilliant-violet-605-anti-mouse-cd19-antibody-7645?GroupID=BLG10556
Pacific Blue-conjugated anti-CD21/35
https://www.biolegend.com/en-us/cell-health/pacific-blue-anti-mouse-cd21-cd35-cr2-cr1-antibody-4336?GroupID=BLG5432
PE/Cyanine7 conjugated anti-CD23
https://www.biolegend.com/en-us/products/pe-cyanine7-anti-mouse-cd23-antibody-3941
PE-conjugated anti-CD5
https://www.biolegend.com/en-us/products/pe-anti-mouse-cd5-antibody-160?GroupID=BLG6762
PerCP-Cy5.5-conjugated anti-IgM
https://www.biolegend.com/en-us/products/percp-cyanine5-5-anti-mouse-igm-4519?GroupID=BLG3548
PE-conjugated anti-CD45.2
https://www.biolegend.com/en-us/cell-health/pe-anti-mouse-cd45-2-antibody-7?GroupID=BLG7007
FITC-conjugated anti-CD45.1
https://www.biolegend.com/en-us/products/fitc-anti-mouse-cd45-1-antibody-198?GroupID=BLG1933
FITC-conjugated anti-CD1d
https://www.biolegend.com/en-us/products/fitc-anti-mouse-cd1d-cd1-1-ly-38-antibody-4319?GroupID=BLG5435
APC-conjugated anti-TER-119
https://www.biolegend.com/en-us/products/apc-anti-mouse-ter-119-erythroid-cells-antibody-1863?GroupID=ImportedGROUP1
FITC-conjugated anti-CD41
https://www.biolegend.com/en-us/products/fitc-anti-mouse-cd41-antibody-5896
PE-conjugated anti-IgD
https://www.biolegend.com/en-us/products/pe-anti-mouse-igd-1379
Pacific Blue-conjugated anti-IgM
https://www.biolegend.com/en-us/search-results/pacific-blue-anti-human-igm-antibody-6637?GroupID=BLG4120
Alexa Fluor 700-conjugated anti-CD1c
https://www.biolegend.com/en-us/products/alexa-fluor-700-anti-human-cd1c-antibody-9864
FITC-conjugated anti-CD27
https://www.biolegend.com/en-us/products/fitc-anti-human-cd27-antibody-8348
Alexa Fluor 647-conjugated anti-IgM
https://www.biolegend.com/en-us/productstab/alexa-fluor-647-anti-mouse-igm-9684?GroupID=BLG3548
APC-conjugated anti-IgMa
https://www.biolegend.com/en-us/products/apc-anti-mouse-igma-antibody-15550
PE-conjugated anti-IgMb
https://www.biolegend.com/en-us/products/pe-anti-mouse-igmb-1745?GroupID=BLG4488
APC Hamster IgG1 isotype control
https://www.bdbiosciences.com/en-us/products/reagents/flow-cytometry-reagents/research-reagents/flow-cytometry-controls-and-lysates/apc-hamster-igg1-isotype-control.553974

Alexa Fluor 647-conjugated anti-Ki-67
https://www.bdbiosciences.com/en-us/products/reagents/flow-cytometry-reagents/research-reagents/single-color-antibodies-ruo/alexa-fluor-647-mouse-anti-ki-67.558615
PE Hamster IgG1 isotype control
https://www.bdbiosciences.com/en-us/products/reagents/flow-cytometry-reagents/research-reagents/flow-cytometry-controls-and-lysates/pe-hamster-igg1-isotype-control.553972
biotinylated anti-IgMa
https://www.bdbiosciences.com/en-us/products/reagents/flow-cytometry-reagents/research-reagents/single-color-antibodies-ruo/biotin-mouse-anti-mouse-igm-a.553515
biotinylated anti-IgMb
https://www.bdbiosciences.com/en-us/products/reagents/flow-cytometry-reagents/research-reagents/single-color-antibodies-ruo/biotin-mouse-anti-mouse-igm-b.553519
biotinylated anti-IgG1a
https://www.bdbiosciences.com/en-us/products/reagents/flow-cytometry-reagents/research-reagents/single-color-antibodies-ruo/biotin-mouse-anti-mouse-igg1-a.553500
biotinylated anti-IgG1b
https://www.bdbiosciences.com/en-us/products/reagents/flow-cytometry-reagents/research-reagents/single-color-antibodies-ruo/biotin-mouse-anti-mouse-igg1-b.553533
PE-conjugated anti-CD55
https://www.miltenyibiotec.com/US-en/products/cd55-daf-antibody-anti-mouse-reafinity-rea300.html#conjugate=pe:size=30-ug-in-1-ml
APC-conjugated anti-CD97
https://www.miltenyibiotec.com/US-en/products/cd97v2-antibody-anti-mouse-reafinity-rea678.html#conjugate=apc:size=30-ug-in-1-ml
Annexin V-FITC
https://www.miltenyibiotec.com/US-en/products/annexin-v-conjugates.html#conjugate=fitc:size=100-tests-in-1-ml
APC-conjugated anti-CD97
https://www.miltenyibiotec.com/US-en/products/cd97-antibody-anti-human-reafinity-rea1242.html#conjugate=apc:size=30-tests-in-60-ul
APC-conjugated anti-CD55
https://www.miltenyibiotec.com/US-en/products/cd55-daf-antibody-anti-human-reafinity-rea1231.html#conjugate=apc:size=30-tests-in-60-ul
AMCA-conjugated donkey anti-goat IgG (H+L)
https://www.jacksonimmuno.com/catalog/products/705-155-147
Peroxidase-conjugated Streptavidin
https://www.jacksonimmuno.com/catalog/products/016-030-084

Eukaryotic cell lines

Policy information about cell lines and Sex and Gender in Research

Cell line source(s)	The Plat-E cell line was a gift from Susan R. Schwab at New York University. HEK293T cell line was originally from ATCC.
Authentication	No specific procedure was taken to authenticate the cell line identity. The Plat-E cell line is selected in puromycin/blasticidin regularly.
Mycoplasma contamination	The cell lines have been tested negative for mycoplasma contamination.
Commonly misidentified lines (See ICLAC register)	No cell line used in this study are in the database of commonly misidentified cell lines.

Animals and other research organisms

Policy information about studies involving animals; ARRIVE guidelines recommended for reporting animal research, and Sex and Gender in Research

Laboratory animals	B6 (NCI 556) and B6-Ly5.2 (CD45.1) (NCI 564) mice were purchased from the National Institute at Charles River at age 6-8 weeks. Mpl −/− (MGI: 3763248) mice were provided by M. R. Looney, University of California, San Francisco (UCSF). Rag1−/− (JAX: 002216; B6.129S7-Rag1tm1Mom/J) mice were provided by A. Ma, UCSF. Mb1-cre mice (JAX: 020505; B6.C(Cg)-Cd79atm1(cre)Reth/EhobJ), IgHa congenic B6 mice (Jax: 001317; B6.Cg-Gpi1a Thy1a Igha/J), Adgre5−/− mice, Cd55−/− mice, Arhgef1−/− mice, Gna13f/f mice, Ubiquitin-GFP mice (JAX: 004353; Tg(UBC-GFP)30Scha/J), and Cd19−/− mice were from the internal colony. All mice were on a C57BL/6 background. All mice were housed in a specific-pathogen free environment at the Laboratory of Animal Research Center at UCSF and all animal procedures were approved by the UCSF Institutional Animal Use and Care Committee. In LARC, time controlled lightling on standard 12:12 light: dark cycle was applied. The humidity and ambient room temperature were maintained at 30% to 40% and 68ºF to 70ºF. Ages (at the time of analysis) of the animals are listed below: Fig. 1 Two-photon imaging was performed on two batches of MZ B cells reconstituted CD19-/- mice, one batch of mice were 18 weeks old, one batch of mice were 16 weeks old.

Fig. 2
1) In Fig. 2d, Adgre5-/- and Adgre5+/- mice were littermates and 11-12 weeks old.
2) In Fig. 2f and g, WT/Adgre5+/+ and WT/Adgre5-/- mixed chimeras were about 17-18 weeks old.
3) In Fig. 2h and i, B6 mice were 9-10 weeks old.
4) In Fig. 2k and i, BM chimeras were 14-15 weeks old.
Fig. 3
1) In Fig. 3b, G13f/f Mb1 cre+ (labeled as Gna13 cKO) mice and their littermate control mice were 10-12 weeks old.
2) In Fig. 3d, WT/Gna13 WT and WT/Gna13 cKO mixed chimeras were about 17-18 weeks old.
3) In Fig. 3e, G13f/f Mb1 cre+ (labeled as Gna13 cKO) mice and their littermate control mice were 8-9 weeks old.
4) In Fig. 3g, Arhgef1+/- and Arhgef1-/- mice were 12 weeks old.
5) In Fig. 3i, WT/Arhgef1+/+ and WT/Arhgef1-/- mixed chimeras were 16-17 weeks old.
Fig. 4
1) In Fig. 4c, CD55+/- and CD55-/- mice were 10-12 weeks old.
2) In Fig. 4e, WT/CD55+/+ and WT/CD55-/- mixed chimeras were about 15-16 weeks old.
3) In Fig. 4f, WT/CD55+/+, WT/dKO and CD55-/-/dKO mixed chimeras were about 17-18 weeks old.
4) In Fig. 4g, CD55+/- and CD55-/- mice were 15-16 weeks old.
5) In Fig. 4h, Mpl-/-/CD55+/- and Mpl-/-/CD55-/- mixed chimeras were 14 weeks old.
Fig. 5
1) In Fig. 5a, CD55+/- and CD55-/- mice were 15-16 weeks old.
2) In Fig. 5d, CD55+/+ and CD55-/- mice were 8 weeks old.
Fig. 7
1) In Fig. 7a, Adgre5-/- and Adgre5+/- mice were littermates and 12-14 weeks old.
2) In Fig. 7b, WT/Adgre5+/+ and WT/Adgre5-/- mixed chimeras were about 17-18 weeks old.
3) In Fig. 7c, Gna13 cKO mice and their littermate control mice were 10-12 weeks old.
4) In Fig. 7d, IgHa WT/IgHb Adgre5+/+ and IgHa WT/IgHb Adgre5-/- mixed chimeras were about 18-19 weeks old.
5) In Fig. 7e and f, IgHa WT/IgHb Adgre5+/+ and IgHa WT/IgHb Adgre5-/- mixed chimeras were about 20-22 weeks old.
6) In Fig. 7g, Adgre5-/- and Adgre5+/- mice were littermates and 13-14 weeks old.
Extended Data Fig. 2
In Extended Data Fig. 2g-j, Adgre5-/- GFP+, Adgre5+/+ GFP and B6 mice were 10-11 weeks old.
Extended Data Fig. 3
In Extended Data Fig. 3e, Gna12+/- and Gna12-/- chimeras were 17 weeks old.
Extended Data Fig. 4
In Extended Data Fig. 4i and j, Rag1-/-/CD55+/+ and Rag1-/-/CD55-/- mixed chimeras were 13 weeks old.
Extended Data Fig. 7
1) In Extended Data Fig. 7a, CD55-/- and littermate control mice were 11-12 weeks old.
2) In Extended Data Fig. 7b, Arhgef1-/- and littermate control mice were 11-12 weeks old.
3) In Extended Data Fig. 7c, WT/Arhgef1+/+ and WT/Arhgef1-/- mixed chimeras were 16 weeks old.

Wild animals	No wild animals was used in this study.
Reporting on sex	The study did not involve sex-biased study. Sex-matched mice were randomly chosen in each experiment.
Field-collected samples	The study did not involve samples collected from the field.
Ethics oversight	All animal procedures were approved by the UCSF Institutional Animal Use and Care Committee.

Note that full information on the approval of the study protocol must also be provided in the manuscript.

Flow Cytometry

Plots

Confirm that:

☒ The axis labels state the marker and fluorochrome used (e.g. CD4-FITC).

☒ The axis scales are clearly visible. Include numbers along axes only for bottom left plot of group (a 'group' is an analysis of identical markers).

☒ All plots are contour plots with outliers or pseudocolor plots.

☒ A numerical value for number of cells or percentage (with statistics) is provided.

Methodology

Sample preparation	Single-cell suspensions of splenic cells were prepared and stained with antibodies of indicated specificities in MACS buffer (PBS and 1% FBS).
Instrument	LSR II or Symphony A1 (BD Biosciences)
Software	Flowcytometry data were collected using BD FACSDIVA V8.0.1 and 9.0.2, and analyzed by FlowJo V10.
Cell population abundance	At least 10000 events were acquired in the defined cell population.

Gating strategy	Dead cell exclusion was based on Fixable Viability Dye eFluor 780 staining (eBioscience) and non-singlet events were excluded with FSC-W/FSC-H characteristics. Isotype control was used to discriminate bwtween background and marker-positive events.

☒ Tick this box to confirm that a figure exemplifying the gating strategy is provided in the Supplementary Information.